# Decomposition of Estuarine Circulation and Residual Stratification under Landfast Sea Ice

HANS BURCHARD,[a] KARSTEN BOLDING,[b] XAVER LANGE,[a] AND ALEXANDER OSADCHIEV[c]

[a] *Leibniz Institute for Baltic Sea Research Warnemünde, Rostock, Germany*
[b] *Bolding and Bruggeman ApS, Asperup, Denmark*
[c] *Shirshov Institute of Oceanology, Russian Academy of Sciences, Moscow, Russia*

(Manuscript received 14 April 2022, in final form 1 September 2022)

ABSTRACT: For Arctic estuaries that are characterized by landfast sea ice cover during the winter season, processes generating estuarine circulation and residual stratification have not yet been investigated, although some of the largest estuaries in the world belong to this class. Landfast sea ice provides a no-slip surface boundary condition in addition to the bottom boundary, such that frictional effects are expected to be increased. For this study of estuarine circulation and residual stratification under landfast sea ice, first, a simple linear analytical model is used. To include tidally varying scenarios, a water-column model is applied with a second-moment turbulence closure to juxtapose free-surface and ice-covered estuaries. Well-mixed and strongly stratified tidally periodic scenarios are analyzed by means of a decomposition of estuarine circulation into contributions from gravitational circulation, eddy viscosity–shear covariance (ESCO), surface stress, and river runoff. A new method is developed to also decompose tidal residual salinity anomaly profiles. Estuarine circulation intensity and tidally residual potential energy anomaly are studied for a parameter space spanned by the Simpson number and the unsteadiness number. These are the major results of this study that will support future scenario studies in Arctic estuaries under conditions of accelerated warming: (i) residual surface drag under ice opposes estuarine circulation; (ii) residual differential advection under ice destabilizes the near-surface flow; (iii) reversal of ESCO during strong stratification does not occur under landfast sea ice; (iv) tidal pumping (s-ESCO) contributes dominantly to residual stratification also with sea ice cover.

SIGNIFICANCE STATEMENT: Our work gives a first qualitative and quantitative understanding of how landfast sea ice cover on tidal estuaries impacts on the generation of estuarine circulation and residual stratification. Along the Arctic coasts, where some of the world's largest estuaries are located, these processes play a significant role for the economy and ecology by means of transports of sediments, nutrients and pollutants. Due to Arctic amplification, the conditions for ice-covered estuaries are strongly changing in a way that the ice-covered periods may be shorter in the future. Our results intend to motivate field observations and realistic model studies to allow for better predicting the consequences of these changes.

KEYWORDS: Ocean; Arctic; Estuaries; Coastal flows

## 1. Introduction

The most studied estuaries in the world do not show any relevant ice cover during the annual cycle, but seasonal ice cover is the case for many Arctic river estuaries. In particular, four out of the six largest estuarine rivers on Earth, namely, the Yenisei, Saint Lawrence, Ob, and Amur Rivers, have seasonal ice cover (Fig. 1). Moreover, ice cover is observed at numerous smaller estuaries with low air temperature during the cold season. In particular, almost all river estuaries located in the Arctic Ocean region are completely frozen in winter and spring.

The classical physical oceanography of tidal estuaries, that is, the brackish water regions in the salt mixing zones between rivers and the coastal ocean, has become a well-established research field during the last decades. The focus of the research has been on processes of mixing and estuarine circulation (MacCready and Geyer 2010; Geyer and MacCready 2014) and its relation to sediment trapping (Burchard et al. 2018) in midlatitude estuaries. These reviews do, however, not discuss dynamics of ice-covered estuaries.

In ice-free tidal estuaries, the generation of estuarine circulation depends on various processes that interact nonlinearly in a complex way (Geyer and MacCready 2014). Gravitational circulation caused by the tidal mean effect of longitudinal density gradients has been long believed to dominate estuarine circulation (Pritchard 1952, 1954, 1956; Hansen and Rattray 1965). Later, estuarine convergence (Ianniello 1979; Burchard et al. 2014), eddy viscosity–shear covariance (ESCO; Jay and Musiak 1994; Burchard and Baumert 1998; Burchard and Hetland 2010; Dijkstra et al. 2017), lateral circulation (Nunes and Simpson 1985; Lerczak and Geyer 2004; Burchard et al. 2011), and wind straining (Weisberg and Sturges 1976; Chen and Sanford 2009; Lange and Burchard 2019) have been recognized as factors substantially impacting on the strength

Denotes content that is immediately available upon publication as open access.

*Corresponding author*: Hans Burchard, hans.burchard@io-warnemuende.de

DOI: 10.1175/JPO-D-22-0088.1


FIG. 1. Segments of continental shoreline with seasonal ice coverage (red lines) in the Northern Hemisphere, as well as locations, annual volumes of river runoff ($Q$), and areas of watershed basins ($S$) of the largest Arctic and subarctic estuaries.

of estuarine circulation. Which of these processes dominates depends on details of the tidal characteristics, river runoff, local topography, and tidal and wind forcing. It should be noted that comparable studies have not been carried out for estuaries covered with landfast sea ice, and it must be assumed that all these relations are largely invalid for such conditions.

Coverage by landfast ice during about half of the year is the important feature of the Arctic estuaries (see section 2); however, little is known about the impact of the ice cover on the estuarine physics. There are only a few studies that investigate such impacts (such as Macdonald and Yu 2006; Georgas 2012; Wang et al. 2012; Mohammadian et al. 2021). The fundamental difference between a free-surface tidal flow and an ice-covered tidal flow has been shown by Georgas (2012) for the upper Hudson River during ice cover: instead of a classical flow profile with a no-slip condition at the bed and maximum flow velocity at the surface, the ice-covered tidal flow is characterized by no-slip conditions at the surface and at the bed, with a flow maximum at middepth, similar to a classical pipe flow. The observations could be reproduced by a numerical model by Georgas (2012). Since the ice cover had been limited to the freshwater reach of the tidal river, no conclusions about effects of ice cover on estuarine dynamics could be made. None of the Arctic estuarine studies investigated the effects of ice cover on estuarine circulation and mixing.

This study extends the approach outlined by Burchard and Hetland (2010), Burchard et al. (2014), and Lange and Burchard (2019) who formally solved the tidally averaged momentum equations to obtain vertical profiles of the tidally averaged velocity profile and its decomposition into contributions from gravitational circulation, ESCO, surface stress (e.g., due to wind forcing), and river runoff. Ice cover is simply parameterized by means of a no-slip condition at the surface. Surface heat and freshwater fluxes are neglected, as well as transitional processes of freezing and melting that lead to generation and removal of landfast sea ice. Wind forcing is neglected in both cases, without and with ice cover (note that for landfast ice cover, any effects of wind forcing should not be transferred to the underlying water column). As in other fundamental one-dimensional studies of estuarine dynamics (e.g., Simpson et al. 2002; Burchard and Hetland 2010) surface buoyancy fluxes are supposed to be much smaller than vertical buoyancy fluxes generated by tidal straining (see Figs. 4d, 6d, 8d, and 9d).

In addition, a new approach is developed to decompose residual salinity anomaly profiles into contributions from different

processes. This is motivated by analytical solutions obtained for a vertically constant eddy viscosity and eddy diffusivity, which allows for polynomial solutions (Hansen and Rattray 1965).

The paper is structured as follows: First, the relevance of ice-covered estuaries is demonstrated for large Arctic estuaries mainly located along the Siberian coast (section 2). Then, one-dimensional budget equations for momentum and salinity are given as basis for the simulations and the analysis (section 3). In section 4, results of the analytical model are briefly presented. As the core of the study, results from the tidally resolving simulations are presented in section 5, where the decomposition of residual profiles is explained in section 5a, nondimensional measures for estuarine circulation and residual stratification are introduced in section 5b, the model setup is explained in section 5c, example tidal scenarios are presented in section 5d, and results from the parameter space study are shown in section 5e. Finally, the results are discussed in section 6, and conclusions are drawn in section 7. The analytical and semianalytical formulations for the decomposition of estuarine circulation and residual stratification are given in the appendix (sections a and b).

## 2. Relevance

### a. Characterization of arctic estuaries

For Arctic estuaries, the duration of the ice coverage lasts half a year or more. Many estuaries located in subpolar and midlatitude areas in the Northern Hemisphere also have seasonal ice coverage. Ice covers estuaries from several weeks to several months at certain shelf sea regions of the Pacific Ocean (Bering Sea, Sea of Okhotsk, Sea of Japan, Bohai Sea, Gulf of Alaska) and the Atlantic Ocean and its marginal seas (Labrador Sea, Hudson Bay, Gulf of Saint Lawrence, Baltic Sea, Sea of Azov, Black Sea), see Fig. 1. Apart from rivers discharging into Northern Hemisphere ice-covered estuaries, a considerable amount of freshwater is entering the Arctic Ocean via river deltas. Examples of such river deltas are the Lena, Indigirka, Kolyma, Yukon, and Mackenzie deltas (Osadchiev et al. 2020b, 2021a; Spivak et al. 2021). Since they are not expected to show a comparable estuarine dynamics, they are not further discussed here.

The Arctic estuaries with the largest annual mean freshwater discharge are the Gulf of Ob (530 $km^3\ yr^{-1}$) and the Yenisei Gulf (630 $km^3\ yr^{-1}$) in the Kara Sea, the Pechora Gulf (130 $km^3\ yr^{-1}$) in the Barents Sea, and the Khatanga Gulf (100 $km^3\ yr^{-1}$) in the Laptev Sea (Osadchiev et al. 2019, 2020a, 2021b,c; Fig. 1). In total, Arctic estuaries provide a river discharge of 2200 $km^3\ yr^{-1}$ including 1600 $km^3\ yr^{-1}$ from large estuaries listed above and 600 $km^3\ yr^{-1}$ from numerous small estuaries in the Barents, Kara, and Laptev Seas (Gordeev et al. 1996). This volume accounts for 6% of total river runoff to the World Ocean (Dai and Trenberth 2002).

### b. Seasonality of discharge in arctic estuaries

The ice season at the Ob, Yenisei, and Khatanga Gulfs lasts from October–November to June–July. During this period, the whole areas of the Yenisei and Khatanga Gulfs are covered by landfast ice (Osadchiev et al. 2020a). The Gulf of Ob is only partly covered by landfast ice because a large polynya occupies the northern part of the gulf (Popov et al. 2016). The White Sea is covered by pack ice from the months of January–February to April–May (Chernov et al. 2018). In addition to the ice coverage in winter, an important feature of the Arctic rivers (in contrast to midlatitude and tropical rivers) is that they have a very short and intense discharge period in summer and very low discharge during the rest of the year (Osadchiev et al. 2021b,c). Up to 75%–80% of the total annual discharge of the Ob and Yenisei Rivers occurs in May–September, in particular, 40%–55% in June–July. The late spring flood wave has a peak elevation of 5 m at the Ob River and even 12 m at the Yenisei River, which is an important hydraulic feature once it reaches the estuary and propagates down to the sea (Pavlov et al. 1996). The estuaries are still covered by ice during this period. Further eastward, the weather conditions in winter–spring are colder and rivers are frozen to the bottom from October to May, which results in zero discharge (Pavlov et al. 1996). For example, the Khatanga River provides 75% of annual discharge in June–July and 100% in June–September (Osadchiev et al. 2020a).

Generally, the Arctic estuaries are poorly studied during the cold season due to a lack of ice-based in situ measurements. In particular, the Gulf of Ob is the only estuary with reliable information about average surface and bottom salinity distribution in winter (Voinov et al. 2017; Fig. 2). The Gulf of Ob shows significant seasonal variability in salinity structure caused by variability of river discharge and ice coverage. In late summer, after the flooding period, river water occupies the whole water column in the southern and central part of the Gulf of Ob (Osadchiev et al. 2021c). A salt-wedge zone with a large salinity gradient between the freshened surface layer and the saline bottom layer is typically located in the northern part of the gulf (72°–72.5°N, Osadchiev et al. 2021c). Surface salinity at this area is 1–5 $g\ kg^{-1}$, while bottom salinity is 5–25 $g\ kg^{-1}$. In winter, river discharge decreases and the gulf is covered by ice. As a result, the salt-wedge zone shifts southward to the central part of the gulf (70.5°–71°N; Voinov et al. 2017). Surface salinity in the northern part of the gulf increases to 15–25 $g\ kg^{-1}$.

The majority of the Gulf of Ob is covered by landfast ice (1–2 m thick) from October/November to June/July (Pavlov et al. 1996). However, a large polynya is formed northward from the landfast ice with an ice thickness of 5–30 cm that occupies the northern part of the gulf during most years (Popov et al. 2016). During very cold winters, landfast ice covers the whole gulf and the polynya is located northward from the gulf in the open sea. Since the polynya is localized in the northern part of the gulf, we assume that it does not modify the large-scale estuarine flow.

### c. Effects of ice cover on tidal intensity

Landfast ice coverage causes a reduction of tidal velocity and elevation amplitudes. In particular, the dominant tidal amplitude $M_2$ decreases from 13–24 cm in July–October to 4–8 cm in November–May in the central part of the Gulf of Ob and from 37–47 to 18–26 cm in the northern part of the

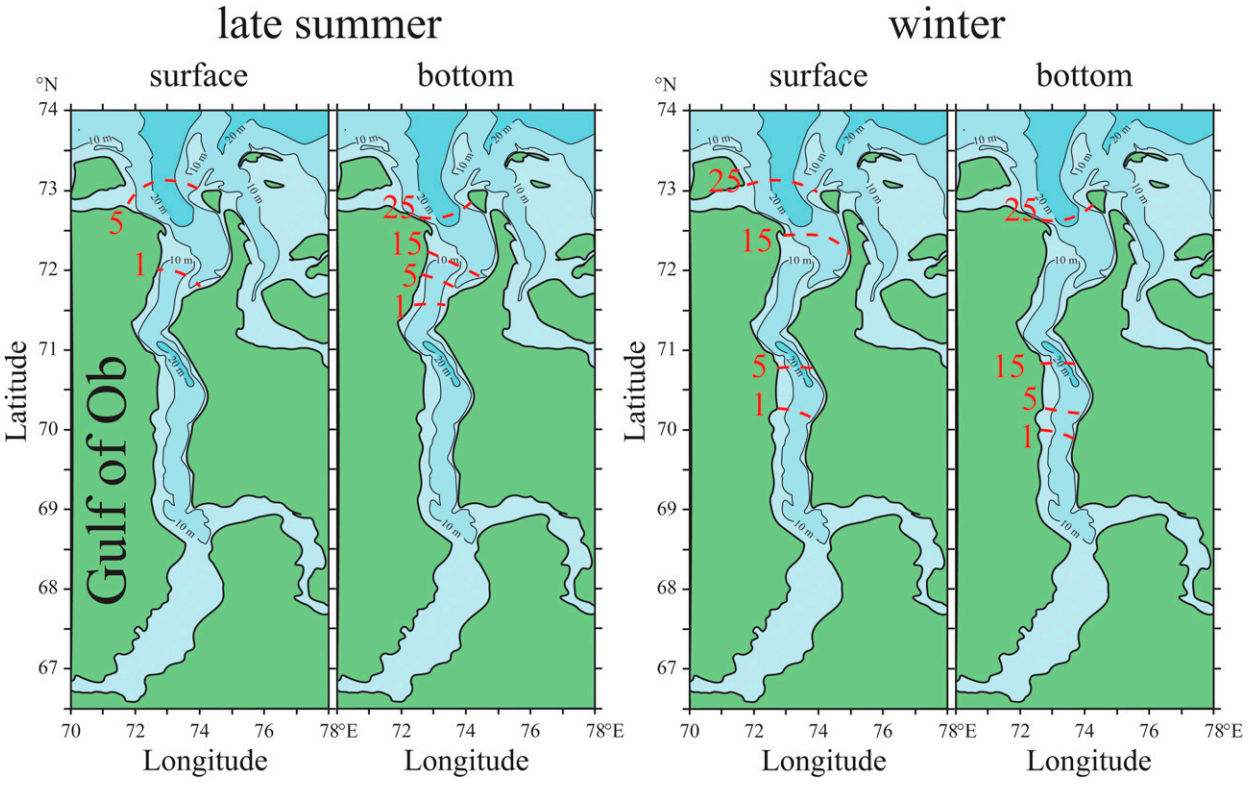


FIG. 2. Average position of isohalines of 1, 5, 15, and 25 g kg$^{-1}$ (red lines and red numbers) in the Gulf of Ob in the surface and bottom layers in (left) late summer and (right) winter. This figure has been adapted from (Voinov et al. 2017) and (Osadchiev et al. 2021c).

gulf (Voinov 2016; Voinov et al. 2017; Voinov and Piskun 2019). The monthly climatology of amplitudes and phases of tidal constituents shows a characteristic distribution for different locations along the Siberian coast and each constituent, which is also reflected in the mean spring range (Kulikov et al. 2020). Typically, the analysis shows a decreasing tidal energy during the first few months of the year, followed by a substantial increase during the ice-free season in summer, which is then decreased again when the ice cover sets in autumn.

The polynya ice coverage also reduces tidal amplitudes, however, to a smaller extent (Voinov and Piskun 2019). Tidally induced horizontal motion of landfast ice in the Gulf of Ob is considered to be small, however, there is no available information about its direct measurement (Tarasenko et al. 2022).

No observations of the tidal velocity amplitude under landfast ice are available for tidal estuaries. Therefore, to include a large range of possible conditions, the present study covers a large parameter space in terms of the nondimensional horizontal buoyancy gradient and the nondimensional tidal velocity amplitude.

## 3. Basic equations

The basic budget equations for momentum and salinity are shown here for both, analytical examples with constant eddy coefficients and numerical examples with eddy coefficients calculated from second-moment closure models.

Temporal (e.g., mostly tidal) averaging is defined as

$$\langle X(z,t)\rangle = \frac{1}{T}\int_{t-T/2}^{t+T/2} X(z,\tau)\, d\tau, \tag{1}$$

with the averaging period $T$. For any quantity $X$, the deviation from the tidal average is denoted as $X' = X - \langle X\rangle$.

### a. Momentum equation

The investigations here are based on the one-dimensional irrotational momentum budget for $u$ with constant in time and space horizontal buoyancy gradient $b_x \geq 0$:

$$\partial_t u - \partial_z(A_v \partial_z u) = -g\partial_x \eta - z b_x, \tag{2}$$

where $A_v$ is the eddy viscosity, $g$ is gravitational acceleration, $\partial_x \eta$ is the surface slope, $t$ is time, and $z$ is the vertical coordinate extending from the bottom at $z = -H$ to the surface that is fixed at $z = 0$. The water depth $H$ is kept constant such that no freezing and melting freshwater fluxes are considered at the surface. Some influence of Earth rotation would be expected, specifically in terms of secondary lateral circulation. This has been shown for the estuarine water-column study by Simpson et al. (2002) already. However, the effects are not so fundamental that the additional dependence of the results on an additional parameter such as the Ekman number would be needed.

With $b_x \geq 0$, the water column is oriented in a way that $u > 0$ represents flood flow (landwards, i.e., toward higher buoyancy and lower salinity, respectively) and $u < 0$ represents ebb flow (seawards, i.e., toward lower buoyancy and higher salinity, respectively).

With (1), tidal averaging of (2) and assuming periodic conditions leads to

$$\partial_z \langle A_v \partial_z u \rangle = g \partial_x \langle \eta \rangle + z b_x, \tag{3}$$

which is the starting point for the decomposition of residual velocity profiles based on two subsequent vertical integrations to obtain profiles of $\langle u \rangle(z)$, see the appendix, sections a(1) and b(1).

The dynamic boundary conditions at the surface and at the bottom are given as upward momentum fluxes,

$$\begin{aligned} -A_v \partial_z u &= -u_{*s} |u_{*s}| = -\frac{\tau_s}{\rho_0}, \quad \text{for } z = 0 \,(\text{surface}), \\ -A_v \partial_z u &= u_{*b} |u_{*b}| = \frac{\tau_b}{\rho_0}, \quad \text{for } z = -H \,(\text{bottom}), \end{aligned} \tag{4}$$

with the surface friction velocity $u_{*s}$, the bottom friction velocity $u_{*b}$, the surface stress $\tau_s$, and the bottom stress $\tau_b$. The notation is such that during flood ($\partial_z u > 0$ near the bottom), a negative bottom momentum flux (momentum is transferred downward into the bottom) is resulting and thus negative bottom friction velocity and stress. At the surface, positive stress and friction velocity (i.e., landward surface stress) coincide with $\partial_z u > 0$ and thus with a negative surface momentum flux and vice versa.

At the bottom, a no-slip condition is assumed that specifies the flux boundary condition:

$$u = 0, \quad \text{for } z = -H \,(\text{bottom}). \tag{5}$$

In the presence of landfast sea ice, a no-slip boundary condition is also assumed for the surface:

$$u = 0, \quad \text{for } z = 0 \,(\text{surface}). \tag{6}$$

The ebb-oriented vertically averaged residual runoff velocity $u^r < 0$ is defined as

$$u^r = \frac{1}{H} \int_{-H}^{0} \langle u(z) \rangle \, dz. \tag{7}$$

### b. Salinity equation

The one-dimensional salinity equation with salinity $s$, horizontal salinity gradient $s_x$, and eddy diffusivity $K_v = A_v / \mathrm{Pr}^t$ (with the turbulent Prandtl number $\mathrm{Pr}^t$) is of the following form:

$$\partial_t s + u s_x - \partial_z (K_v \partial_z s) = -\frac{s - s_n}{T_n}, \tag{8}$$

with zero-flux boundary conditions at the surface and the bottom:

$$\begin{aligned} -K_v \partial_z s &= 0, \quad \text{for } z = 0 \,(\text{surface}), \\ -K_v \partial_z s &= 0, \quad \text{for } z = -H \,(\text{bottom}). \end{aligned} \tag{9}$$

With the linear equation of state for potential density,

$$\rho = \rho_0 [1 + \beta (s - s_0)], \tag{10}$$

and buoyancy

$$b = -g \frac{\rho - \rho_0}{\rho_0}, \tag{11}$$

with the haline contraction coefficient $\beta > 0$, the constant reference salinity $s_0$ and the constant reference density $\rho_0$, we obtain the horizontal salinity gradient

$$s_x = -\frac{1}{g\beta} b_x < 0. \tag{12}$$

Temperature variations are neglected here, since due to the horizontal salinity gradient, salinity effects on density are supposed to be dominant.

In (8), $T_n > 0$ is a nudging time scale and $s_n$ is a spatially and temporally constant target salinity value, such that the term on the right-hand side is a nudging term that parameterizes all unresolved processes (such as lateral circulation) that allows for periodically oscillating salinity profiles in three-dimensional models. Without this term, tidally averaged salinity would be subject to a steady drift. Tidal averaging of (8) gives

$$\frac{\Delta s}{T} + \langle u \rangle s_x - \partial_z \langle K_v \partial_z s \rangle = -\frac{\langle s \rangle - s_n}{T_n}, \tag{13}$$

with the shift in salinity during one tidal cycle $\Delta s$ that is assumed to be depth independent. Vertical averaging of (13) gives

$$\Delta s = -T \left( u^r s_x + \frac{\overline{\langle s \rangle} - s_n}{T_n} \right), \tag{14}$$

where $\overline{\langle s \rangle}$ is the tidally and vertically averaged salinity. Equation (14) shows that for no nudging ($T_n \to \infty$) a negative (freshening) salinity drift $\Delta s = -T u^r s_x < 0$ will occur during each tidal cycle. With nudging (finite $T_n > 0$), the model results performed here converge toward a periodically oscillating solution with $\Delta s = 0$ and $\overline{\langle s \rangle} = s_n - T_n u^r s_x$. Smaller nudging time scales $T_n$ will result in faster convergence toward a periodic state. All simulations in this study are evaluated in such a periodic state.

The tidally averaged salinity budget is the basis for the derivation of solutions for the residual salinity anomaly profiles for constant eddy coefficients [appendix section a(2)] and eddy coefficients calculated from a second-moment turbulence closure model [appendix section b(2)].

## 4. Analytical model

Here, analytical solutions for residual velocity and salinity budgets with constant eddy coefficients [see appendix sections a(1) and a(2) for the derivation] are discussed for scenarios without and with landfast sea ice cover. For a stress-free surface (no wind stress, no ice cover) the classical solutions for

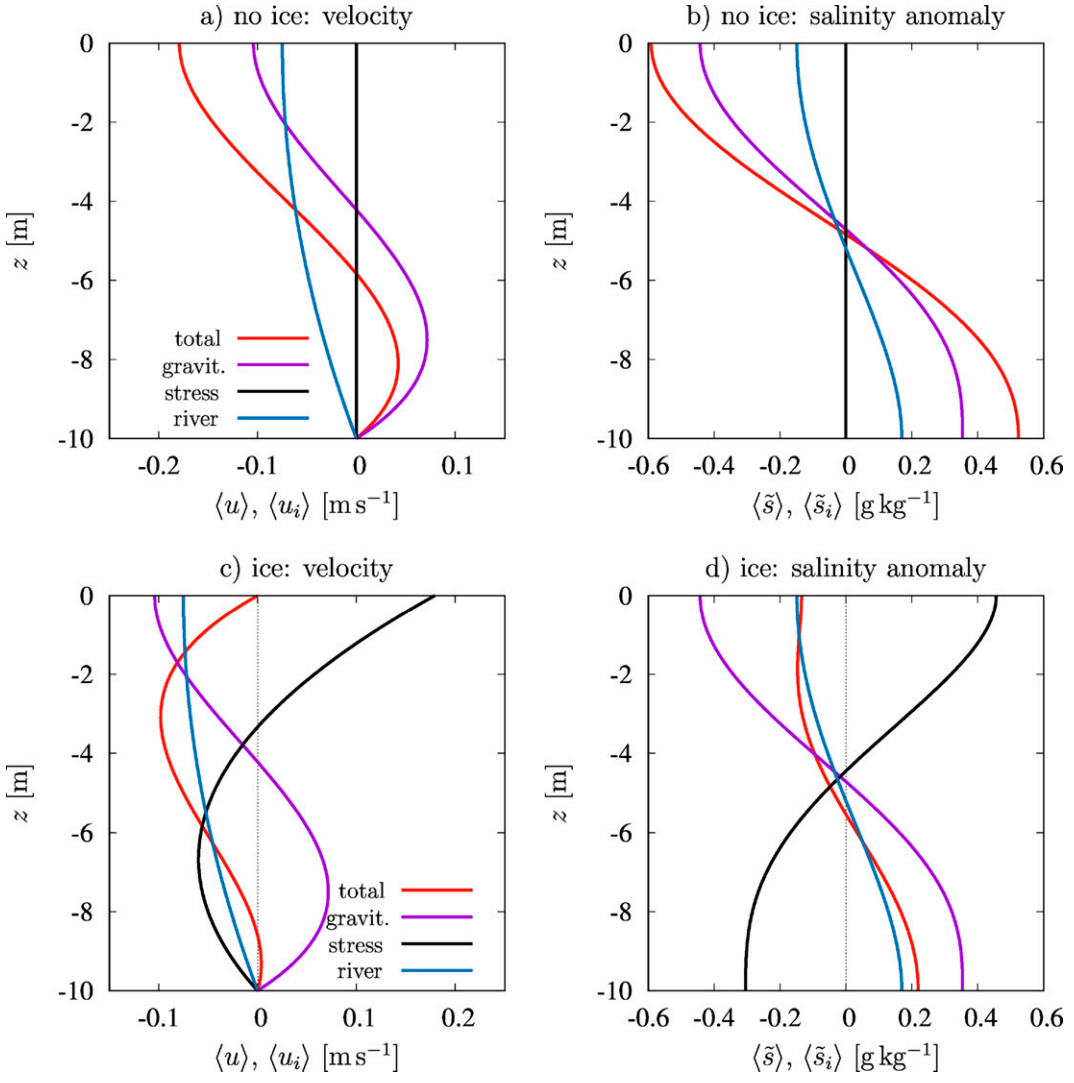


FIG. 3. Analytical solution with constant eddy viscosity and eddy diffusivity: (a),(c) Decomposition of residual velocity and (b),(d) residual salinity anomaly for (top) ice-free and (bottom) ice-covered conditions. Here, the following parameters were used: $A_v = 10^{-3}$ m$^2$ s$^{-1}$, Pr$^t$ = 0.7, $b_x = 5 \times 10^{-6}$ s$^{-2}$, $\beta = 7 \times 10^{-4}$ g$^{-1}$ kg, $H = 10$ m, and $u^r = -0.05$ m s$^{-1}$.

estuarine circulation are obtained, composed of the stratifying effects of gravitational circulation and river runoff (Figs. 3a,b). When, however, a no-slip condition is applied to the sea surface to parameterize the effect of landfast sea ice, an additional component due to surface stress is added, forcing a strong reverse estuarine circulation component (Figs. 3c,d), while the other contributions to the momentum and salinity anomaly profiles remain unchanged for the same river discharge and horizontal buoyancy gradient. Note that we here use the term *reverse* instead of *inverse* to avoid confusion with evaporation-dominated inverse estuaries. The reason is the positive surface stress (i.e., downward surface momentum flux) needed to enforce the no-slip surface condition by increasing the negative surface velocity to zero. This reverse circulation component has the effect that the estuarine circulation is substantially decreased (red curve in Fig. 3c). Furthermore, due to the positive near-surface shear, the differential salinity advection leads to an unstably stratified salinity anomaly profile near the surface (red curve in Fig. 3d). Such an instability of the residual salinity profile can only exist in this simple analytical model due to the missing feedback to the eddy diffusivity. In the tidally varying model, the eddy coefficients will strongly increase in such a situation such that the instability will be largely removed, leading to well-mixed surface profiles [section 5d(2)].

Our analysis uses a no-slip bottom and an ice-free (and stress-free) sea surface as a starting point and considers the situation with landfast sea ice as a special case where a surface stress guarantees a no-slip condition at all times. This leads to the surface stress-related profiles as additional components of the residual velocity and salinity anomaly profiles. Even for a

scenario without horizontal buoyancy gradient, for which residual profiles would be symmetric around middepth, the decomposition is not symmetric. This is a consequence of the method chosen that focuses on the extra surface stress needed for the surface no-slip condition. This asymmetry of the decomposition is also present in the time-varying scenarios presented in section 5.

## 5. Tidally resolved dynamics

For investigating tidally resolved water-column scenarios, periodically oscillating simulations using the General Ocean Turbulence Model (GOTM, www.gotm.net; Burchard et al. 1999; Li et al. 2021) are carried out and analyzed, as already done in previous studies of idealized tidal flow (Burchard 2009; Burchard and Hetland 2010; Lange and Burchard 2019). Simulations without and with sea ice cover are juxtaposed.

To force a tidal current, the surface slope $\partial_x \eta$ is varied in a way that the vertically averaged velocity results as

$$\overline{u}(t) = \frac{1}{H}\int_{-H}^{0} u(t,z)\, dz = u^r + u^t \sin(\omega t), \tag{15}$$

with the tidal velocity amplitude $u^t$ and the tidal frequency $\omega$; see Burchard and Hetland (2010) for details.

### a. Decomposition of residual profiles

For all simulations, tidally averaged velocity profiles are decomposed into contributions from gravitational circulation, ESCO, surface stress-induced circulation and runoff circulation. This analysis has first been proposed by Burchard and Hetland (2010) and is summarized in appendix section b(1) of the present study. All these exchange flow profiles have a zero vertical average, except for the circulation due to runoff, which has a vertical average of $u^r$. The procedure for calculating this decomposition is in principle the same as for the analytical decomposition derived in appendix section a(1) and analyzed in section 4. The difference here is that (i) the resulting expressions need to be numerically evaluated due to the high complexity in time and space and (ii) the decomposition contains one extra term due to the temporal ESCO that does not occur for constant-in-time eddy viscosity profiles. In summary, the residual velocity profiles are decomposed into these contributions:

- $\langle u_1 \rangle$: ESCO.
- $\langle u_2 \rangle$: Gravitational circulation (gravit.).
- $\langle u_3 \rangle$: Surface-stress circulation (stress).
- $\langle u_4 \rangle$: Circulation due to river runoff (river).
- $\langle u_5 \rangle$: Residual circulation due to nonperiodicity and discretization errors (error).

Equivalently to the analytical decomposition, also the residual salinity anomaly profiles (A11) obtained for the tidal scenarios are decomposed. This is a method that is developed here for the first time, see details in appendix section b(2). First of all, the residual salinity anomaly decomposition consists of the advective contributions from the decomposed residual velocity profile, that is, the gravitational circulation, ECSO, surface stress circulation and runoff circulation. Moreover, the contribution from the temporal covariance between eddy diffusivity and vertical salinity gradient (s-ESCO) is included, which could also be denoted as *tidal pumping*. Finally, the contribution from salinity nudging is included. In summary, the residual salinity anomaly profiles are decomposed into these contributions:

- $\langle \tilde{s}_1 \rangle$: Advective contribution from ESCO.
- $\langle \tilde{s}_2 \rangle$: Advective contribution from gravitational circulation (gravit.).
- $\langle \tilde{s}_3 \rangle$: Advective contribution from surface-stress circulation (stress).
- $\langle \tilde{s}_4 \rangle$: Advective contribution from river runoff (river).
- $\langle \tilde{s}_5 \rangle$: Contribution from s-ESCO.
- $\langle \tilde{s}_6 \rangle$: Contribution from nudging (nudging).
- $\langle \tilde{s}_7 \rangle$: Residual circulation due to nonperiodicity and discretization errors (error).

### b. Nondimensional parameters and measures

The most relevant nondimensional parameters of the estuarine flow are the Simpson number Si (nondimensional horizontal buoyancy gradient, representing the ratio of stratifying to mixing forces, Simpson et al. 1990; Stacey et al. 2010) and the unsteadiness number Un (nondimensional tidal period, representing the ratio of the water depth to the depth of the bottom boundary layer, Baumert and Radach 1992; Burchard and Hetland 2010) with

$$\mathrm{Si} = \frac{b_x H^2}{\langle u_{*,b}^2 \rangle}; \quad \mathrm{Un} = \frac{\omega H}{\langle u_{*,b}^2 \rangle^{1/2}}, \tag{16}$$

where $\langle u_{*,b}^2 \rangle$ is the tidally averaged square bed friction velocity. An alternative way of defining these parameters had been introduced by Burchard (2009) to include the mixing effect of surface stress. Instead of the bottom friction velocity, he used the root sum of the bottom and surface friction velocity squares as the friction velocity scale. As discussed in section 5e, the concept would have failed here, since the critical value of Si for the transition between mixed and stratified scenarios for ice-covered estuaries would have been significantly below unity.

The nondimensional intensity of the exchange flow is quantified as

$$\hat{M} = -\frac{4}{Hu^t}\int_{-H}^{0} \langle u(z) \rangle \left(\frac{z}{H} + \frac{1}{2}\right) dz;$$
$$\hat{M}_i = -\frac{4}{Hu^t}\int_{-H}^{0} \langle u_i(z) \rangle \left(\frac{z}{H} + \frac{1}{2}\right) dz, \tag{17}$$

see Lange and Burchard (2019). The measures $\hat{M}$ and $\hat{M}_i$ are defined in a way that a hypothetical exchange flow with $u/u^t = \hat{u}_0$ in the lower half of the water column and $u/u^t = -\hat{u}_0$ in the upper half of the water column results in $\hat{M} = \hat{u}_0$, such that for classical estuarine circulation $\hat{M} > 0$ and for inverse circulation $\hat{M} < 0$ is obtained. Furthermore, the measure is additive in a way that $\hat{M} = \sum_i \hat{M}_i$ for $[u(z)] = \sum_i [u_i(z)]$.

A suitable measure for the water-column stability is the potential energy anomaly (Simpson 1981; Burchard and Hofmeister 2008), which reads in nondimensional form as

$$\hat{\phi} = \frac{\phi}{\rho_0 b_x H^2} = \frac{1}{b_x H^3}\int_{-H}^{0} z\tilde{b}\, dz',$$
$$\hat{\phi}_i = \frac{\phi_i}{\rho_0 b_x H^2} = \frac{1}{b_x H^3}\int_{-H}^{0} z\tilde{b}_i\, dz', \qquad (18)$$

where $\tilde{b} = -g\beta\tilde{s}$ and $\tilde{b}_i = -g\beta\tilde{s}_i$ are the buoyancy anomalies corresponding to the salinity anomaly and its decomposition. With this, $\phi$ is the amount of energy needed to vertically homogenize a stratified water column with $\phi > 0$ indicating a stably stratified water column and $\phi < 0$ indicating an unstably stratified water column. As for with $M$, also this measure is additive in a way that $\hat{\phi} = \sum_i \hat{\phi}_i$ since $\langle\tilde{s}(z)\rangle = \sum_i \langle\tilde{s}_i(z)\rangle$.

### c. Model setup

Eddy viscosity and eddy diffusivity are calculated by means of a two-equation $k - \varepsilon$ turbulence closure model with an algebraic second-moment closure, as documented by Umlauf and Burchard (2005). The closure model uses budget equations for the turbulent kinetic energy per unit mass (TKE) $k$ and its dissipation rate $\varepsilon$. To parameterize the effect of unresolved breaking of internal waves and to avoid unrealistically small values of the TKE under stably stratified conditions, a minimum value of $k_{\min} = 10^{-7}$ J kg$^{-1}$ has been used, together with limiting the size of energetic eddies by the Ozmidov scale $L_O = (\varepsilon/N^3)^{1/2}$ (see Burchard and Bolding 2001, for details), with the dissipation rate $\varepsilon$ and the buoyancy frequency $N$.

In real estuaries, the bottom roughness length $z_0^b$ can vary by several orders of magnitude due to properties of the seabed such as sediment type and bed forms (Wright et al. 1987). The effective roughness length may also depend on the flow direction since bed forms can be asymmetric due to ebb or flood dominance (Herrling et al. 2021). The roughness length $z_0^s$ at the interface between landfast sea ice and the water column can vary over orders of magnitude as well, depending on the properties of the ice (McPhee et al. 1987; Mellor and Kantha 1989). From their velocity profile observations in the freshwater reach of the Hudson River estuary Georgas (2012) estimated a roughness length of $z_0^s = 4.4 \times 10^{-4}$ m, mentioning that this might be an upper value for this estuary. In the present idealized model study, for simplicity, we chose $z_0^b = z_0^s = 1.0 \times 10^{-4}$ m.

To allow for periodic solutions and avoid nonperiodic runaway stratification (Blaise and Deleersnijder 2008) also for strongly stable stratification, nudging of salinity to a constant background salinity of $s_n = 15$ g kg$^{-1}$ using a nudging time scale of $T_n = 44\,714$ s (equal to the semidiurnal lunar tidal period $M_2$) has been applied according to (8). Considerably shorter nudging time scales would lead to too well-mixed salinity profiles (and increasing contributions of the nudging term). Much longer time scales would still lead to runaway stratification for strongly stratified situations. By doing so, unresolved three-dimensional processes guaranteeing periodicity are parameterized. The model is initialized from rest (zero velocity, minimum values for turbulent quantities) and at a vertically homogeneous salinity of $s = s_n = 15$ g kg$^{-1}$. It should, however, be noted that the choice of the initial conditions does not have an effect on the periodic state that we analyze.

Sufficient numerical accuracy for calculating the decomposition of residual velocity and salinity anomaly profiles requires a high numerical resolution in time and space. Therefore, the water column of $H = 10$ m is vertically discretized with 400 layers with zooming toward the surface and the bottom, such that the vertical increments vary between $\Delta z = 7.5 \times 10^{-3}$ m at the surface and the bottom and $\Delta z = 4 \times 10^{-2}$ m at middepth. The time step is $\Delta t = M_2/20\,000 = 2.2357$ s. All scenarios are simulated for 20 tidal periods, of which the last one is analyzed for tidal averages. With this, it is guaranteed that the simulation is in a periodic equilibrium. For all residual velocity and salinity anomaly profiles the residual error (including the nonperiodicity and the numerical truncation error) is calculated and shown to be sufficiently small.

### d. Example tidal scenarios

#### 1) Without ice cover

A tidally resolved example for a weakly stratified, tidal energetic scenario without ice cover is given in Fig. 4. The dimensional parameters and the resulting nondimensional parameters and exchange flow and stratification measures are given in the caption. The value of the Simpson number of Si = 0.78 indicates the presence of strain-induced periodic stratification (SIPS; Simpson et al. 1990) with well-mixed or weakly unstable conditions during later stages of the flood current and marginally stable conditions during ebb. This can best be seen in Fig. 4d, where the buoyancy production is largely positive during flood (potential energy is converted to TKE), apart from an active entrainment of the turbulent layer into stratified surface water during the first half of the flood. Buoyancy production is negative during ebb (TKE is used to reduce water-column stability). This tidal asymmetry leads to high eddy viscosity (Fig. 4c) and eddy diffusivity during flood, leading to ESCO (Jay and Musiak 1994; Burchard and Hetland 2010; Dijkstra et al. 2017), which is an important process of generating estuarine circulation in well-mixed tidal estuaries. Figure 4 compares well to Fig. 2 of Burchard and Hetland (2010), which reflects a SIPS situation observed (Rippeth et al. 2001) and simulated (Simpson et al. 2002) in Liverpool Bay.

The decomposition of tidally averaged velocity and salinity anomaly profiles is shown in Figs. 5a,b. The velocity profile decomposition is similar to the same decomposition carried out by Burchard and Hetland (2010), see their Fig. 9 (upper-right panel). In agreement with the study by Burchard and Hetland (2010) also here, the ESCO contribution is about twice as large as the contribution from gravitational circulation, see Table 1, where $\hat{M}_1 = 0.030$ and $\hat{M}_2 = 0.015$ for the weak stratification scenario without ice cover. The newly introduced decomposition of the salinity anomaly profile (48) reveals that most of the stratification is explained by the tidal pumping term $\tilde{s}_5$ (s-ESCO), see Table 2 for the weak stratification scenario without ice cover with $\hat{\phi} = 3.72$ and $\hat{\phi}_5 = 3.06$.

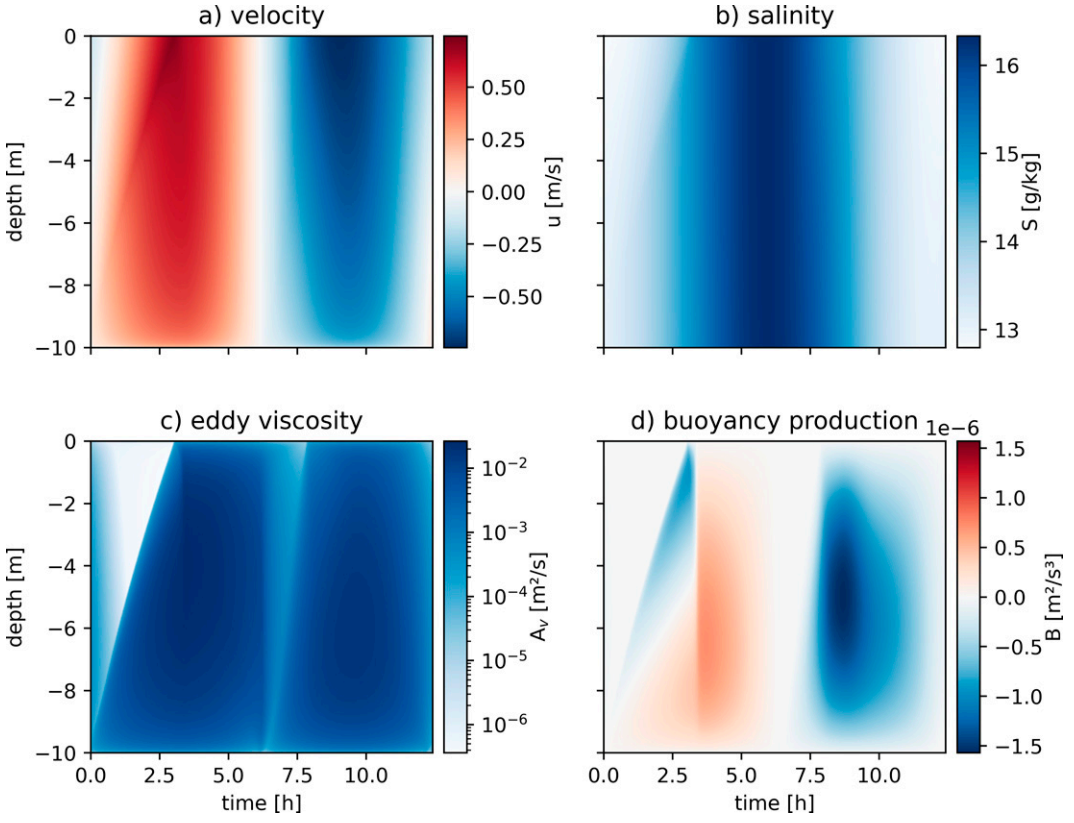


FIG. 4. GOTM results without ice cover. Here, the following parameters were used: $s_x = -4 \times 10^{-4}$ g kg$^{-1}$ m$^{-1}$, $H = 10$ m, $u^t = 0.5$ m s$^{-1}$, and $u^r = -0.02$ m s$^{-1}$. The resulting nondimensional parameters are Si = 0.78 and Un = 0.072, and the measures for exchange flow intensity and stratification are $\hat{M} = 0.050$ and $\hat{\phi} = 3.72$ , respectively.

Although periodicity would not have been obtained without nudging, the nudging contribution to stratification is relatively weak with $\hat{\phi}_6 = 0.08$.

For strong stratification with Si = 1.71, exchange flow and stratification are substantially changed. Stratification is stable throughout the simulation, with a halocline at about $z = -2$ m (Fig. 6). The bottom-to-top salinity difference is about 15 g kg$^{-1}$ (Fig. 6b). Due to the strong stratification and the lack of surface stress, the eddy viscosity in the surface layer is very small and shows little variation during the tidal cycle (Fig. 6c). This low top-layer turbulence in concert with the horizontal density gradients leads to a near-surface exchange flow that leads to a flood velocity maximum at the halocline (Fig. 6a). The cycle of buoyancy production below the halocline is comparable to the situation for weak stratification, with negative values at the top of the entrainment layer during flood and negative values due to marginal stability during ebb, whereas positive values dominate during ebb due to marginal stability forced by tidal ebb straining (Fig. 6d). The estuarine circulation ($\hat{M} = 0.460$) results largely from a balance of gravitational circulation ($\hat{M}_2 = 0.860$) and reverse ESCO circulation ($\hat{M}_1 = -0.467$), see Fig. 7a. The dominant balance for stratification is given by the stratifying process of gravitational circulation ($\hat{\phi}_2 = 2 \times 10^5$) and the destratifying effects of advection due to ESCO ($\hat{\phi}_1 = -1.3 \times 10^5$) and due to unresolved processes of destratification that are parameterized by means of nudging ($\hat{\phi}_6 = -0.9 \times 10^5$). It should, however, be noted for this scenario that the single contributions to the balance are up to two orders of magnitude larger than the total stratification $\hat{\phi} = 187$. The error itself due to nonperiodicity and numerical inaccuracies, $\hat{\phi}_7 = -224$, is comparable to the total stratification $\hat{\phi}$. However, the value of the total (and stable since $\hat{\phi} > 0$) stratification is certain since it is a direct result from the simulation, even though the values of the individual contributions contain some uncertainties.

### 2) WITH ICE COVER

With landfast sea ice cover, the estuarine tidal flow changes its character substantially. The no-slip condition at the surface generates a near-surface boundary layer that acts in the same way as the bottom boundary layer. Therefore, despite a small asymmetry introduced through the horizontal density gradient and the river runoff, the velocity profiles are almost symmetric with respect to middepth for both weak and strong stratification (Figs. 8a and 9a), as shown before for the ice-covered freshwater range of the tidal Hudson River (Georgas 2012). The major consequence of the surface no-slip condition is that near-surface tidal straining is opposed to near-bottom tidal straining: during flood stable stratification is generated ($B < 0$) and during ebb unstable stratification is generated

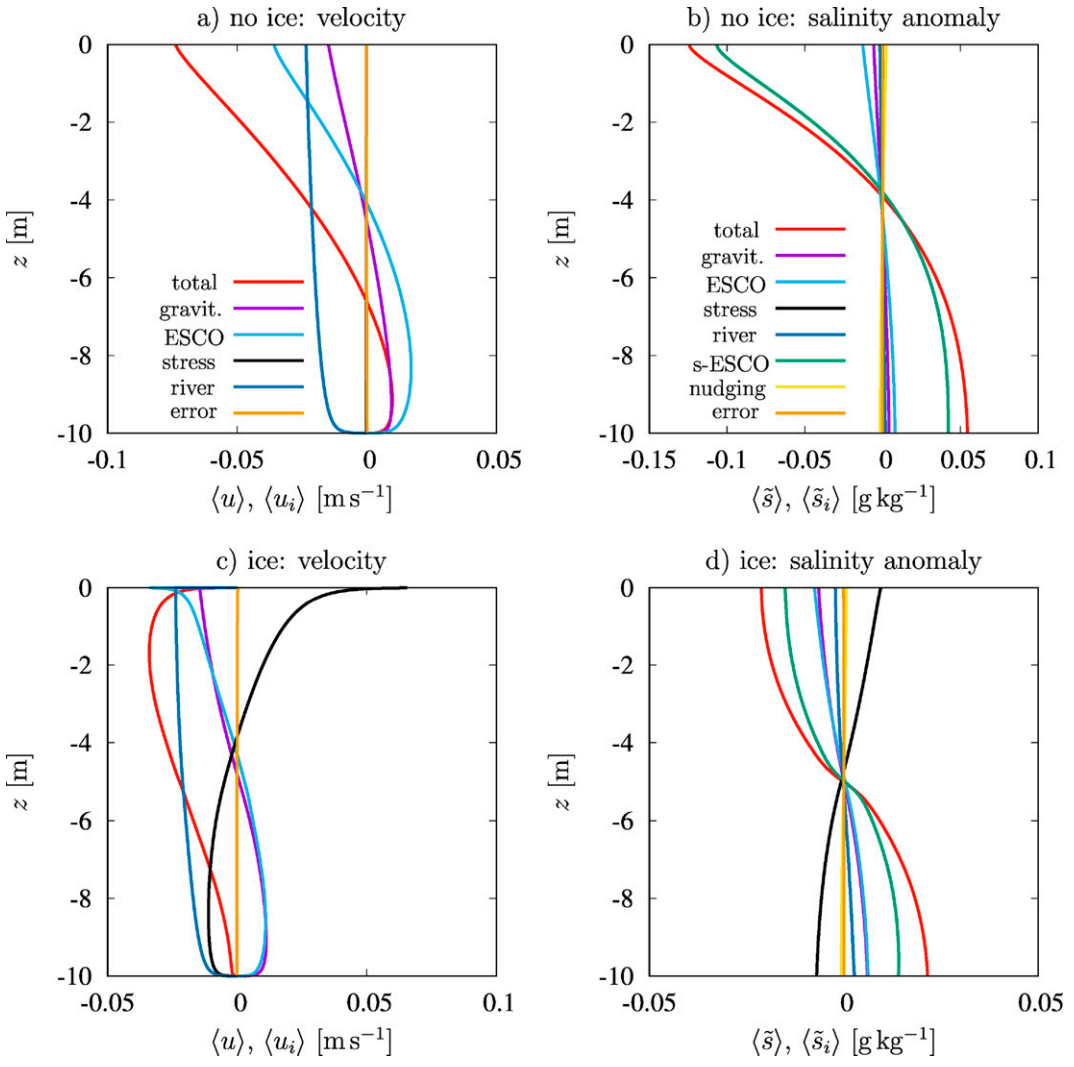


FIG. 5. GOTM simulations for relatively weak stratification, see details in Table 1: (a),(c) Decomposition of residual velocity and (b),(d) residual salinity anomaly for (top) ice-free and (bottom) ice-covered conditions.

(Figs. 8d and 9d). This leads to bottom-enhanced eddy viscosity during flood (same as for no ice cover) and to surface-enhanced eddy viscosity during ebb (Figs. 8c and 9c). In the same way, also eddy diffusivity is enhanced (not shown), a process that will lead to homogenization of the salinity profiles at the surface and the bottom. However, the surface salinity should be even more homogenized than the bottom salinity due to the addition effect of differential advection by the river runoff.

The major difference between weak and strong stratification is the strong halocline at middepth, which is moving upward due to entrainment into the low-turbulence near-surface flood region during flood and vice versa during ebb (Fig. 9b).

TABLE 1. Simpson number and unsteadiness number and the nondimensional exchange flow intensity of the mean velocity profile and its components computed for the weakly and strongly stratified scenarios shown in Figs. 5 and 7.

| Scenario | Si | Un | Total $\hat{M}$ | ESCO $\hat{M}_1$ | Gravit. $\hat{M}_2$ | Stress $\hat{M}_3$ | River $\hat{M}_4$ | Error $\hat{M}_5$ |
|---|---|---|---|---|---|---|---|---|
| No ice, weak stratification | 0.78 | 0.072 | 0.050 | 0.030 | 0.015 | 0.000 | 0.005 | 0.000 |
| With ice, weak stratification | 0.63 | 0.065 | 0.020 | 0.018 | 0.017 | −0.021 | 0.006 | 0.000 |
| No ice, strong stratification | 1.71 | 0.106 | 0.460 | −0.467 | 0.860 | −0.000 | 0.078 | −0.011 |
| With ice, strong stratification | 1.46 | 0.098 | 0.063 | 0.045 | 0.088 | −0.088 | 0.018 | 0.000 |

TABLE 2. Nondimensional potential energy anomaly of the salinity anomaly profile and its components computed for the weakly and strongly stratified scenarios shown in Figs. 5 and 7.

| Scenario | Total $\hat{\phi}$ | ESCO $\hat{\phi}_1$ | Gravit. $\hat{\phi}_2$ | Stress $\hat{\phi}_3$ | River $\hat{\phi}_4$ | s-ESCO $\hat{\phi}_5$ | Nudging $\hat{\phi}_6$ | Error $\hat{\phi}_7$ |
|---|---|---|---|---|---|---|---|---|
| No ice, weak stratification | 3.72 | 0.45 | 0.22 | 0.00 | 0.07 | 3.06 | −0.08 | 0.00 |
| With ice, weak stratification | 1.14 | 0.33 | 0.31 | −0.38 | 0.11 | 0.80 | −0.03 | 0.00 |
| No ice, strong stratification | 187.65 | −12 511.98 | 19 831.29 | 0.00 | 1666.75 | 16.00 | −8590.62 | −223.80 |
| With ice, strong stratification | 11.90 | 3.78 | 8.43 | −8.06 | 1.68 | 8.63 | −2.59 | 0.03 |

Compared to the situation without ice cover, the ice cover creates a reverse estuarine circulation component to enforce the no-slip condition at the surface (Figs. 5c and 7c). This has already been demonstrated for the simple analytical solution shown in Fig. 3c. For the weak stratification, ice cover reduces estuarine circulation from $\hat{M} = 0.050$ to $\hat{M} = 0.020$ (Table 1), such that there is no landward residual flow near the bed (Fig. 5c). In comparison to the ice-free surface, the ESCO contribution is strongly reduced and is of similar size than the contribution from gravitational circulation (which in turn is slightly increased from $\hat{M}_2 = 0.015$ to $\hat{M}_2 = 0.017$ due to reduced tidally averaged eddy viscosity, see Table 1). For the strong stratification, estuarine circulation is reduced from $\hat{M} = 0.460$ to $\hat{M} = 0.063$, leading to a strongly reduced landward near-bottom residual flow component (Fig. 7c).

For the weak stratification scenario, stratification is strongly reduced from $\hat{\phi} = 3.72$ to $\hat{\phi} = 1.14$ by ice cover due to several processes, despite the increased advective effect of gravitational circulation ($\hat{\phi}_2 = 0.31$ vs $\hat{\phi}_2 = 0.22$). First of all, for weak stratification, s-ESCO (tidal pumping) is strongly reduced ($\hat{\phi}_5 = 0.80$ vs $\hat{\phi}_5 = 3.06$). Second, surface-stress related advective straining with $\hat{\phi}_3 = -0.38$ opposes the stratifying agents, see also Fig. 7b.

For the scenario with strong buoyancy forcing, ice cover reduces stratification by a factor of 18 from $\hat{\phi} = 187$ to $\hat{\phi} = 12$

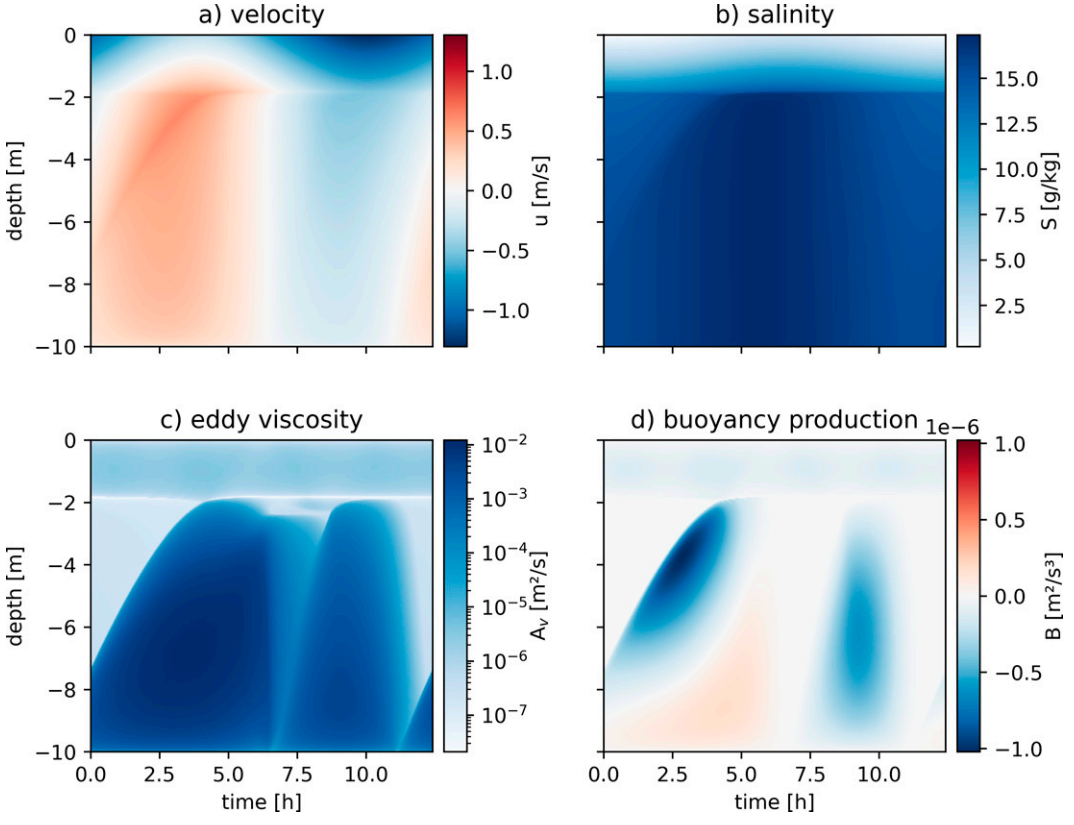


FIG. 6. GOTM results for strong stratification without ice cover. Here, the following parameters were used: $s_x = -4 \times 10^{-4}$ g kg$^{-1}$ m$^{-1}$, $H = 10$ m, $u^t = 0.4$ m s$^{-1}$, and $u^r = -0.02$ m s$^{-1}$. The resulting nondimensional parameters are Si = 1.71 and Un = 0.106, and the measures for exchange flow intensity and stratification are $\hat{M} = 0.460$ and $\hat{\phi} = 187.12$ , respectively.

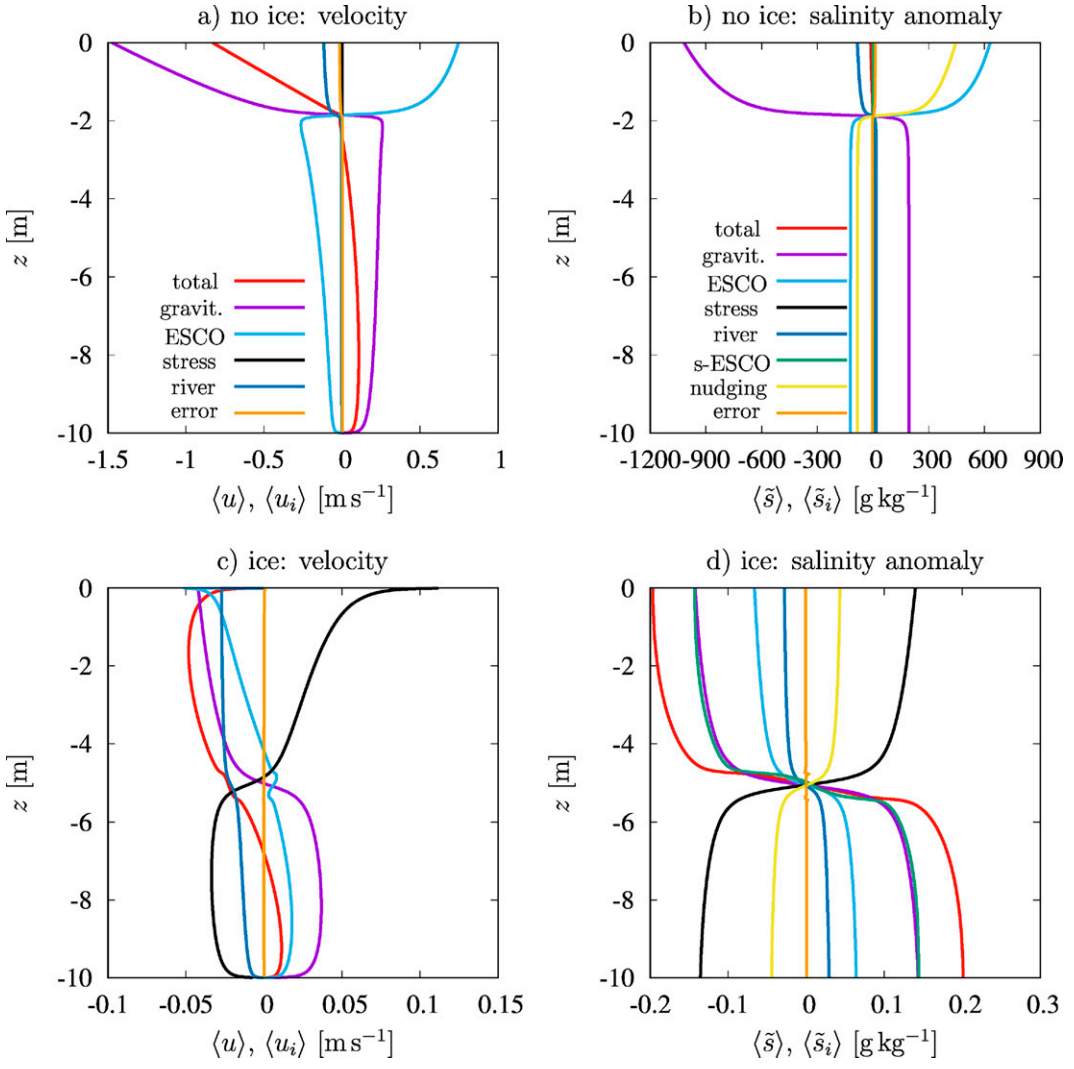


FIG. 7. As in Fig. 5, but for relatively strong stratification, see details in Table 1.

(Table 2). The major balance is between the stratifying forces of s-ESCO ($\hat{\phi}_5 = 8.63$), advection due to gravitational circulation ($\hat{\phi}_5 = 8.43$), and ESCO ($\hat{\phi}_1 = 3.78$) on one hand and the destratifying agent of advection due to surface stress ($\hat{\phi}_5 = -8.06$) and nudging ($\hat{\phi}_6 = -2.59$), see also Fig. 7d.

### e. Parameter space study

To get a clearer picture about the composition of exchange flow and stratification in ice-free and ice-covered tidal estuaries and its variability, a parameter space study is carried out with variations in the Simpson number Si and the unsteadiness number Un. The variation of these two nondimensional parameters is obtained from (16) by systematically varying the buoyancy gradient $b_x$ and the root of the tidally averaged friction velocity square $\langle u_{*,b}^2 \rangle^{1/2}$:

$$b_x = \frac{\mathrm{Si}\,\omega^2}{\mathrm{Un}^2}; \quad \langle u_{*,b}^2 \rangle^{1/2} = \frac{\omega H}{\mathrm{Un}}. \tag{19}$$

Since $\langle u_{*,b}^2 \rangle$ is a result of the simulation rather than an external parameter, it needs to be pre-estimated by means of the tidal velocity amplitude $u^t$:

$$\langle u_{*,b}^2 \rangle = \frac{1}{T}\int_{t-T/2}^{t+T/2} u_{*,b}^2 \, d\tau \approx \frac{1}{T}\int_{t-T/2}^{t+T/2} c_d \overline{u}^2 \, d\tau \approx \frac{c_d (u^t)^2}{T}\int_{t-T/2}^{t+T/2} \sin^2(\omega\tau) d\tau$$

$$= \frac{c_d (u^t)^2}{2}, \tag{20}$$

with the depth-mean drag coefficient

$$c_d = \left[\frac{\kappa}{\ln\left(\frac{H/2 + z_0^b}{z_0^b}\right)}\right]^2, \tag{21}$$

where $z_0^b$ is the bottom roughness length and $\kappa = 0.4$ is the van Kármán constant. With

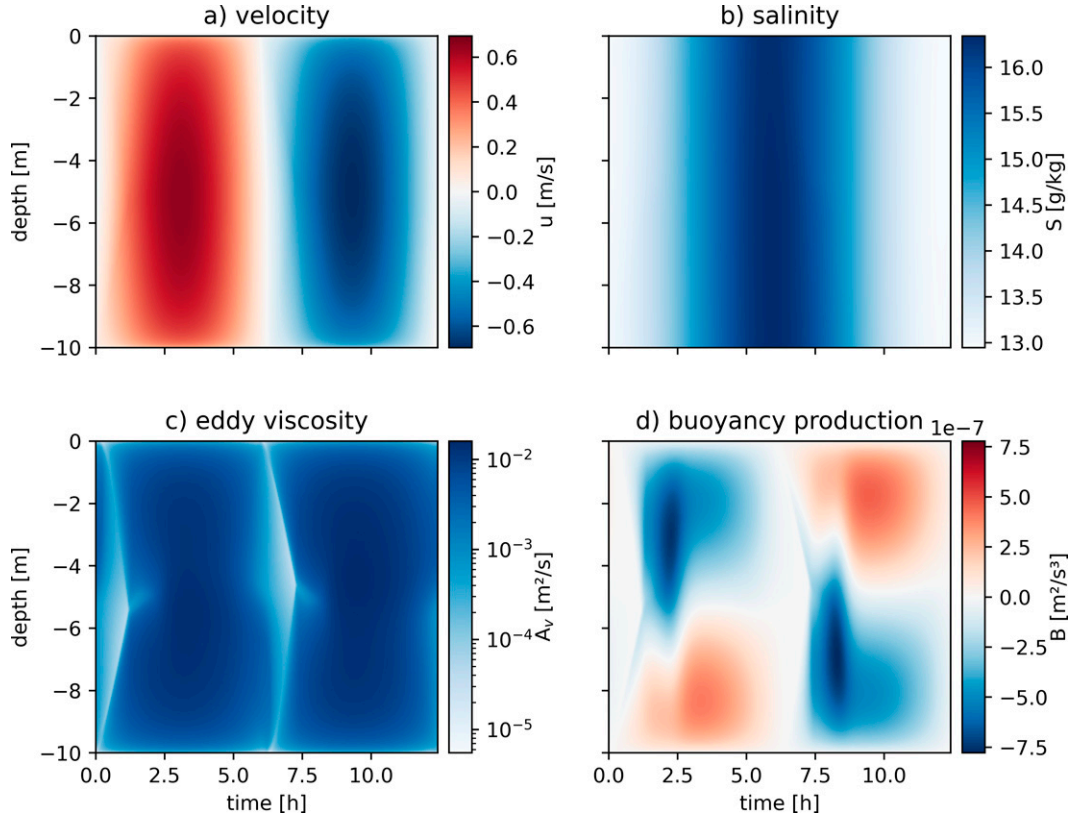


FIG. 8. As in Fig. 4, but with ice cover. The nondimensional parameters are Si = 0.63 and Un = 0.065, and the measures for exchange flow intensity and stratification are $\hat{M} = 0.020$ and $\hat{\phi} = 1.14$ , respectively.

$$u^t \approx \frac{\sqrt{2}\omega H}{\sqrt{c_d}\mathrm{Un}}, \tag{22}$$

the parameter space study is carried out in the following way:

1) A preliminary grid is prescribed with $\overline{\mathrm{Un}}_i = i/i_{\max} \times \overline{\mathrm{Un}}_{\max}$ and $\overline{\mathrm{Si}}_j = j/j_{\max} \times \overline{\mathrm{Si}}_{\max}$ for $i = 0 \ldots i_{\max}$ and $j = 0 \ldots j_{\max}$ with $i_{\max} = 245$ and $j_{\max} = 430$. The parameters $(u^t)_i$ and $(b_x)_{i,j}$ are then calculated using (19) and (22).
2) Using the variables $(u^t)_i$ and $(b_x)_{i,j}$ together with other constant dimensional parameters such as $H = 10$ m, $\omega = 1.405 \times 10^{-4}\,\mathrm{s}^{-1}$ (semidiurnal lunar $M_2$ tide), $T_n = 2\pi/\omega$ and $z_0^b = z_0^s = 10^{-3}$ m (with the surface roughness length $z_0^s$) the water-column calculations are carried out.
3) From each individual simulation, $\langle u_{*,b}^2 \rangle$ is diagnosed and the corresponding corrected values for Si and Un are calculated.
4) The nondimensional measures $\hat{M}$ and $\hat{\phi}$ are analyzed as well as their components. These results are then displayed graphically as color shade plots for the range $0.03 \le \mathrm{Un} \le 0.3$ and $0 \le \mathrm{Si} \le 2$. Table 3 shows the dimensional values of $b_x$, $\langle u_{*,b}^2 \rangle^{1/2}$, and $u^t$ for these corner points. All values outside this range are not shown.

Following these steps, the dimensional buoyancy gradient $b_x$ and the dimensional tidal velocity values $u^t$ at the corner points of the UnSi parameter space are given in Table 3. Both the horizontal buoyancy gradient and the tidal velocity amplitude vary by about one order of magnitude. We expect that a large part of the real conditions of estuarine dynamics are covered. The tidal velocity amplitudes estimated for the northern part of the Gulf of Ob (see section 2c) are at the low end of this parameter space, those in the central part are slightly outside the parameter space. The values observed in the ice-covered tidal river part of the Hudson River by Georgas (2012) with $b_x = 0$ are covered as well. The results are shown in Figs. 10–13.

For ice-free estuaries, a first inspection of the parameter space diagrams for exchange flow intensity (Fig. 10a) and stratification (Fig. 12a) shows a clear transition between weak stratification (small Si) and strong stratification (large Si) at about Si = 1.2, which is largely independent of Un. This critical value is consistent with the $\mathcal{O}(1)$ estimate by Monismith et al. (1996) for the trade-off between the stratifying force of the horizontal density gradient and the destratifying force of the tidal stress. The actual value of this critical Simpson number will depend on the local conditions of the estuary, such as the role of lateral circulation. In the highly idealized one-dimensional scenarios investigated here, the critical value will depend on nondimensional parameters such as the bed roughness parameter $z_0^b/H$ and the nudging time scale $T_n\omega$. Interestingly, a comparable critical value for the Simpson number does also exist for ice-covered estuaries, see Figs. 11a and 13a.

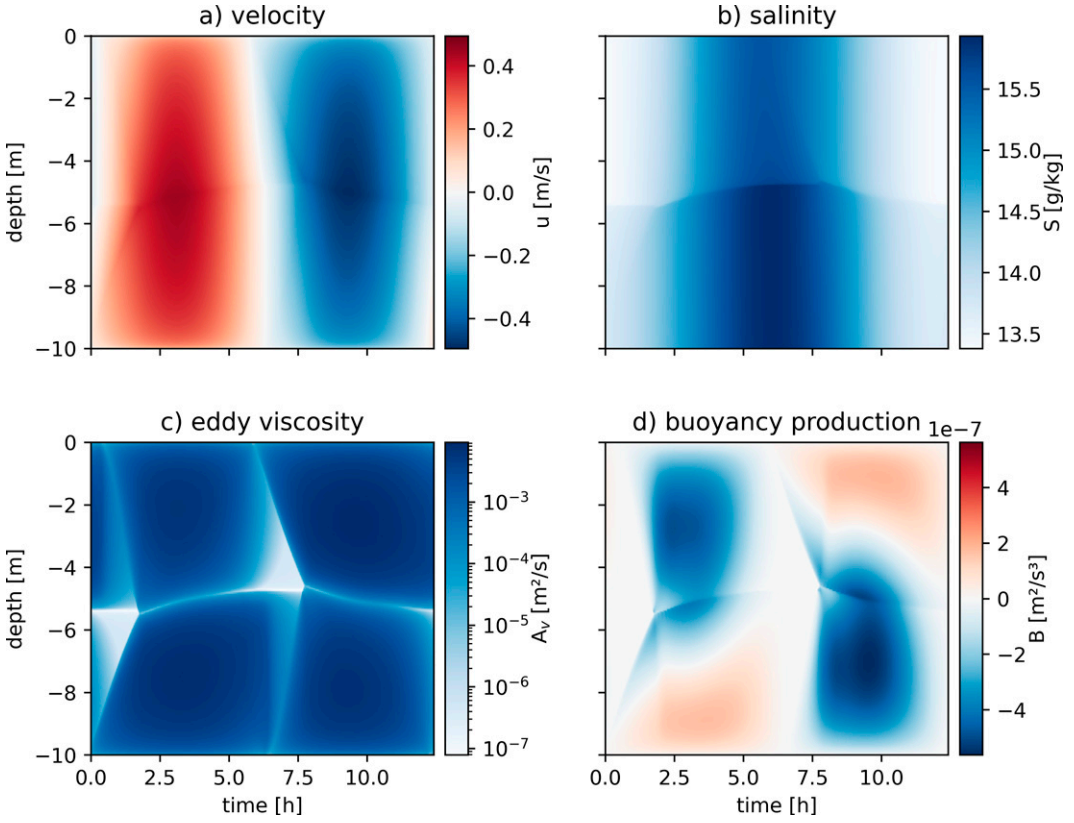


FIG. 9. As in Fig. 6, but with ice cover. The nondimensional parameters are Si = 1.46 and Un = 0.098, and the measures for exchange flow intensity and stratification are $\hat{M} = 0.063$ and $\hat{\phi} = 11.90$ , respectively.

This threshold is not as sharp as for an ice-free estuary, and it increases slightly with Un, but it is clearly identifiable by pronounced gradients of $\hat{M}$ and $\hat{\phi}$ with respect to Si.

Without ice cover, results for weakly stratified tidal flow are comparable to those by Burchard and Hetland (2010), although in that study nudging of salinity had not been applied, leading to runaway stratification for increased Si. Note that Burchard and Hetland (2010) scaled Si and Un with the tidal velocity amplitude instead of the root-mean-square friction velocity, such that a different range of values is used for these parameters. In both studies, ESCO circulation decreases with increasing Un and increases with Si up to a point close to the switch to stable stratification (marked by runaway stratification in Burchard and Hetland 2010), where it does strongly decrease, see Fig. 4 of Burchard and Hetland (2010) and Fig. 10b of the present study. The dependence on Si can be explained by decreasing tidally averaged eddy viscosity $\langle A_v \rangle$ for increasing stratification. A weaker ESCO for larger Un (i.e., larger nondimensional frequency) is due to the fact that for high-frequency tidal forcing the bottom-boundary layer (BBL) height is shallower than for low-frequency tidal forcing where the BBL has more time to develop. Thus, the tidal asymmetry is reduced. For strong stratification, the ESCO circulation is reversed and compensates parts of the strongly increased gravitational circulation, as already reported by Burchard et al. (2011). In contrast to ESCO, the gravitational circulation is only weakly depending on Un.

Without ice cover, the decomposition of stratification corresponds to the strengths of the estuarine circulation components

TABLE 3. Dimensional buoyancy gradient $b_x$ and the dimensional tidal velocity values $u^t$ at the corner points of the Un–Si parameter space.

| | | Without ice | | | With ice | | |
|---|---|---|---|---|---|---|---|
| Un | Si | $b_x$ (s$^{-2}$) | $\langle u_{*,b}^2 \rangle^{1/2}$ (m s$^{-1}$) | $u^t$ (m s$^{-1}$) | $b_x$ (s$^{-2}$) | $\langle u_{*,b}^2 \rangle^{1/2}$ (m s$^{-1}$) | $u^t$ (m s$^{-1}$) |
| 0.03 | 0.0 | 0.00 | $4.68 \times 10^{-2}$ | 1.41 | 0.00 | $4.68 \times 10^{-2}$ | 1.29 |
| 0.30 | 0.0 | 0.00 | $5.64 \times 10^{-3}$ | 0.17 | 0.00 | $5.64 \times 10^{-3}$ | 0.15 |
| 0.03 | 2.0 | $4.28 \times 10^{-5}$ | $4.68 \times 10^{-2}$ | 2.32 | $4.28 \times 10^{-5}$ | $4.68 \times 10^{-2}$ | 1.37 |
| 0.30 | 2.0 | $6.21 \times 10^{-7}$ | $5.64 \times 10^{-3}$ | 0.16 | $6.21 \times 10^{-7}$ | $5.64 \times 10^{-3}$ | 0.16 |

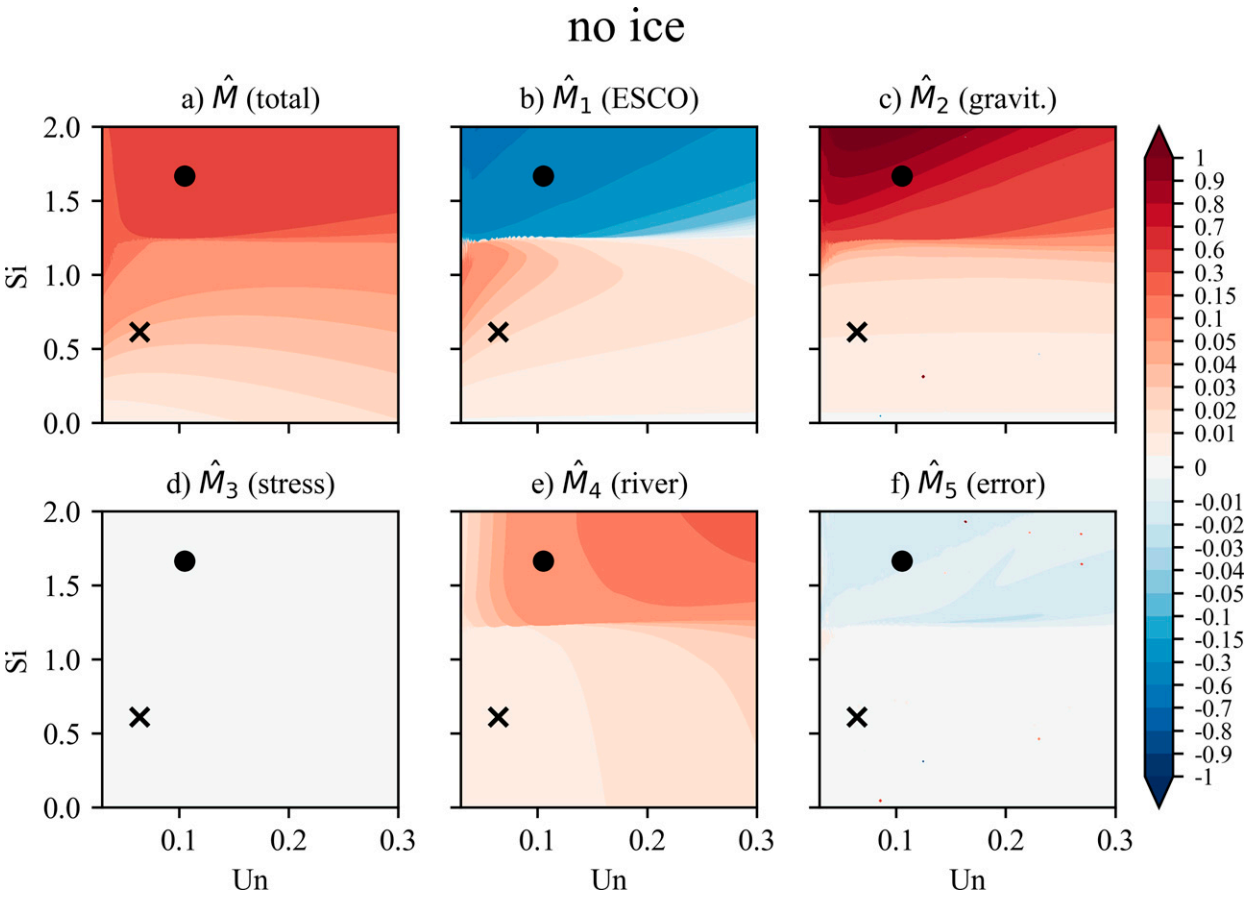


FIG. 10. Ice-free surface: Exchange flow parameter $\hat{M}$ and its components $\hat{M}_1$ (ESCO), $\hat{M}_2$ (gravitational circulation), $\hat{M}_3$ (surface stress circulation), $\hat{M}_4$ (river runoff circulation), and $\hat{M}_5$ (error). The black dot marks the strongly stratified scenario and the black cross marks the weakly stratified scenario, see section 5d. Red colors denote positive estuarine circulation, and blue colors denote reverse estuarine circulation. Note the nonlinear color scale.

(ESCO, gravitational circulation, and runoff circulation), see Figs. 12b, 12c, and 12e. Additionally, tidal pumping (or s-ESCO, see Fig. 12f) is strongly supporting stratification. This process is significantly decreasing with Un, that is, with decreasing tidal asymmetry. In contrast, nudging of salinity toward well-mixed conditions reduces stratification (Fig. 12g). Also notable is the error due to nonperiodicity and numerical discretization, which increases with stratification (Fig. 12h). This error is of the order of the total stratification, but orders of magnitude smaller than the individual contributions (see also Table 2). Since the total stratification $\hat{\phi}$ is exactly diagnosed, the term $\hat{\phi}_7$ indicates the sum of the errors of the other individual contributions $\hat{\phi}_2$–$\hat{\phi}_6$.

When the surface is ice covered, the situation changes completely. Estuarine circulation (Fig. 11a) and stratification (Fig. 13a) are much weaker. This is clearly expressed by the negative contribution from surface stress (Figs. 11d and 13d). Again, all processes are enhanced with increasing Si, again due to decreased tidally averaged eddy viscosity $\langle A_v \rangle$. ESCO and surface stress circulation are generally enhanced by increasing Un, which is in contrast to the ice-free estuary. The processes that contribute to stratification in addition to the advective contributions of ESCO, gravitational circulation, surface stress circulation and runoff circulation (Figs. 13b,c,d,e) have similar contribution as for an ice-free tidal flow: s-ESCO supports stratification and increases with Si and decreases with Un (Fig. 13f) and nudging weakens stratification with increasing Si and largely independently of Un (Fig. 13g). The error stratification is relatively small (Fig. 13h).

## 6. Discussion

The presence of landfast sea ice on top of an estuarine water column has a number of dynamic consequences that result in a completely different tidal cycle of momentum and stratification and substantially changed residual profiles result.

### *a. Residual surface drag under ice opposes estuarine circulation*

The results presented in sections 4 and 5 show that landfast sea ice cover changes the character of the estuarine circulation substantially. This is already evident from a highly simplistic linear model with constant eddy coefficients: the no-slip surface condition for momentum causes a tidally averaged

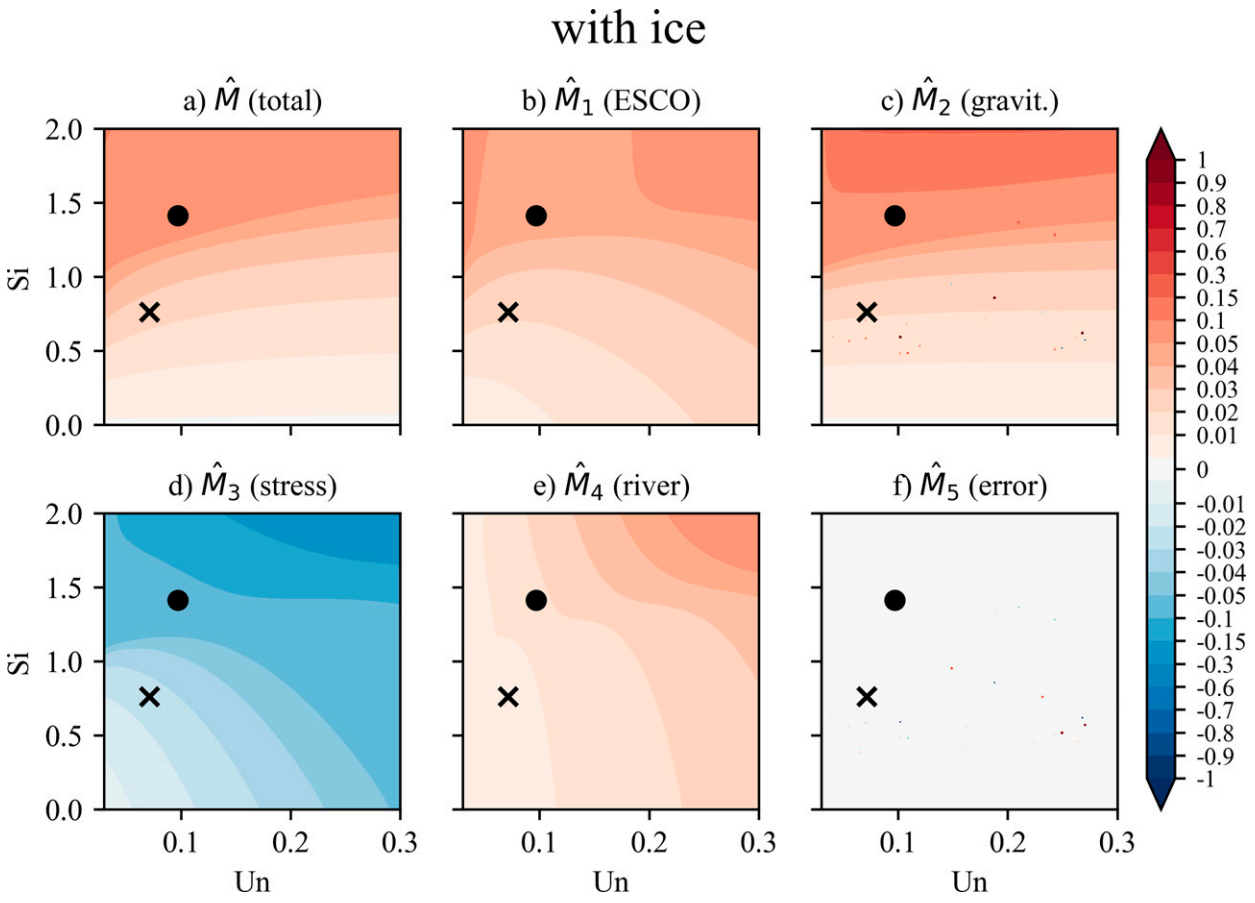


FIG. 11. As in Fig. 10, but for an ice-covered surface.

landward surface drag that opposes the seaward surface flow created by gravitational circulation (Fig. 3). This landward surface drag creates a reverse estuarine circulation component in the same way as an up-estuarine wind stress would do (Geyer 1997; Lange et al. 2020). Thus, estuarine circulation under landfast sea ice is strongly reduced but not reversed, as shown in (A7).

In principle, the situation is similar for tidal flow with variable eddy coefficients. The major difference is that now vertical shear and salinity gradients under landfast sea ice covary with the eddy coefficients. These processes add various mechanisms to the generation of residual flow and salinity anomaly profiles. The main process shown in the model with constant eddy coefficients, that is, the tidally averaged landward surface drag acting against the estuarine circulation to fulfil the no-slip condition, is the same also for the model with tidally varying eddy coefficients. Except that, with varying coefficients, the unstable net surface stratification found in the analytical case is homogenized, as explained in section 6b.

### b. *Residual differential advection under ice destabilizes the near-surface flow*

Another important process that is already revealed by the simple linear model is the destabilization of the near-surface flow under landfast sea ice. The residual velocity under the ice has positive shear (decreasing with depth), such that by means of differential advection it transports less salty up-estuarine water underneath more salty surface water, a process that leads to a positive salinity anomaly gradient (unstable stratification, Fig. 3d).

The residual velocity profiles for the model with tidally varying eddy coefficients do show strongly mixed but not statically unstable conditions near the surface for the weak stratification case (Fig. 5d). For both weak and strong stratification, during flood tidal straining destabilizes the near-bottom waters similarly to for no ice cover. In contrast, during ebb near surface waters are destabilized due to tidal straining under the ice. Ebb and flood conditions are almost mirrored (Figs. 8 and 9), with a slightly more pronounced destabilization during ebb flow, which is additionally enhanced by river runoff (Figs. 8d and 9d).

### c. *Reversal of ESCO during strong stratification does not occur under landfast sea ice*

For an ice-free surface, the reversal of the ESCO circulation for the strong stratification scenarios is a prominent feature (Figs. 7a and 10b). A weakening of the ESCO circulation for conditions close to runaway stratification has already been

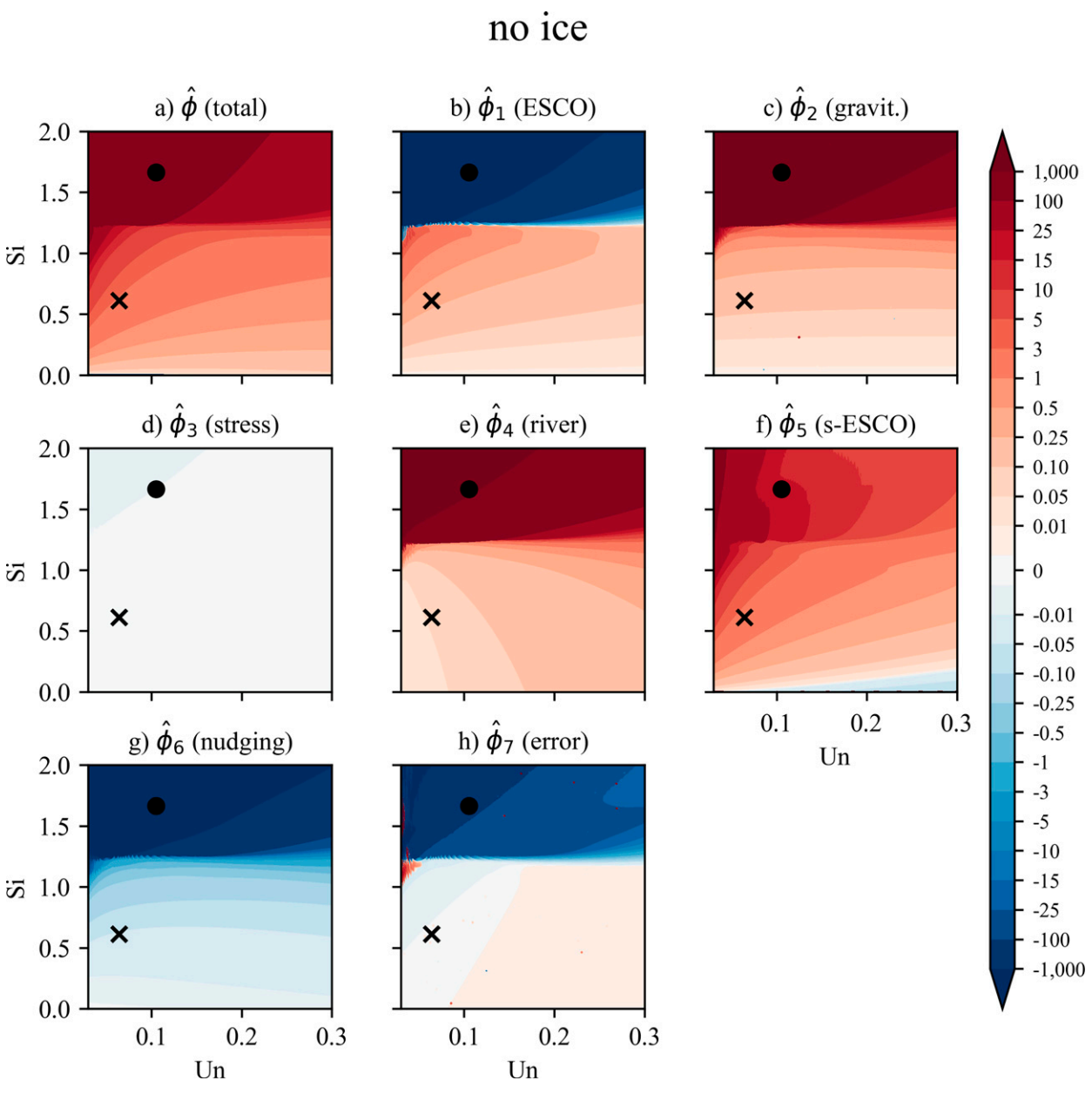


FIG. 12. Ice-free surface: Stratification parameter $\hat{\phi}$ and its components $\hat{\phi}_1$ (advective ESCO contribution), $\hat{\phi}_2$ (advection gravitational contribution), $\hat{\phi}_3$ (advective surface stress contribution), $\hat{\phi}_4$ (advective river runoff contribution), $\hat{\phi}_5$ (tidal pumping, s-ESCO), $\hat{\phi}_6$ (nudging), and $\hat{\phi}_7$ (error). The black dot marks the strongly stratified scenario and the black cross marks the weakly stratified scenario, see section 5d. Red colors denote stabilizing contributions, and blue colors denote destabilizing contributions. Note the nonlinear color scale.

shown by Burchard and Hetland (2010) for their one-dimensional simulations, see their Fig. 4. For two-dimensional cross-sectional simulations, a reversal had been detected by Burchard et al. (2011) for relatively strong stratification (see the large Si scenario in their Table 2). Since those previous studies did not apply nudging to a constant salinity runaway stratification did already occur for relatively low values of Si. The explanation for the reversal of ESCO given by Burchard et al. (2011) is, however, not convincing in hindsight. They related this to a negative covariance of shear and eddy viscosity in the highly stratified near-surface region. However, in the nonturbulent stratified surface layer, shear and eddy viscosity are both very small, such that their covariance $\langle A'_v \partial_z u' \rangle$ should also be small compared to the highly turbulent bottom layer where their covariance is positive (high eddy viscosity and shear anomalies during flood and vice versa during ebb). Furthermore, the river runoff profile (dark blue line in Fig. 7a) is concentrated on the stratified surface, as well as the nondimensional runoff profile $\gamma$, see (A17). A close inspection of the

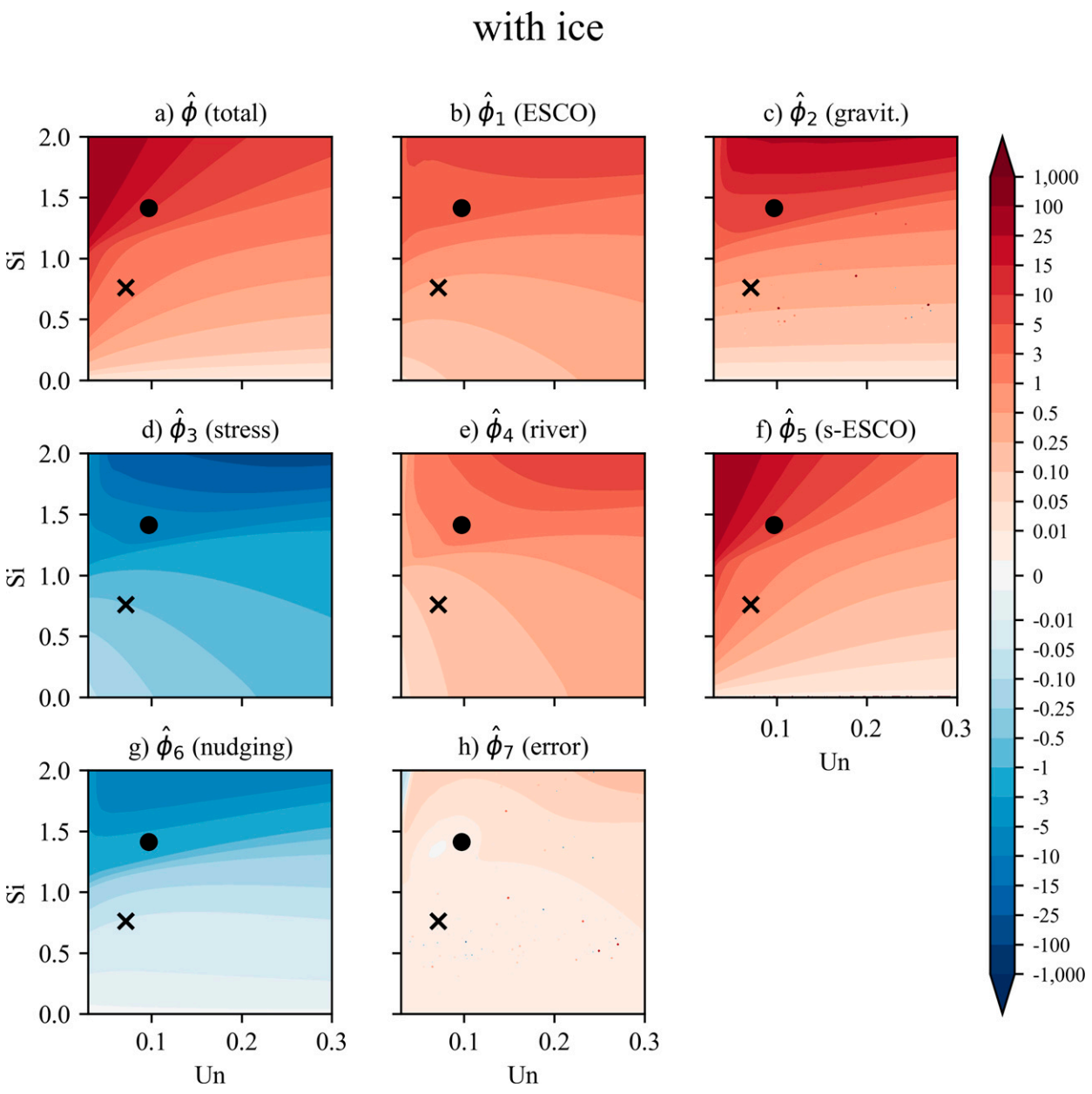


FIG. 13. As in Fig. 12, but for an ice-covered surface.

formulation for the ESCO profile, see (A15) for $i = 1$ shows that the ESCO profile should be negative in the turbulent bottom boundary layer and highly positive near the surface, a shape that leads to negative $\hat{M}_1$ and therefore to a reverse ESCO circulation profile. What can be concluded here is that during strong stratification when estuarine circulation is substantially enhanced, ESCO residual circulation is reversed.

For an ice-covered estuary, there is no tendency visible for a reversal of ESCO residual circulation (Figs. 7c and 11b), although gravitational circulation increases with stratification also for Si > 1.5 (Fig. 11c), but ESCO circulation does not. At this point, it can be concluded that due to the reverse surface stress circulation component estuarine circulation is not strong enough to allow for a reversal of ESCO when estuaries are ice-covered.

### *d. s-ESCO contributes dominantly to residual stratification also with sea ice cover*

The new method of decomposing residual stratification reveals for the first time the substantial role of s-ESCO for the tidally averaged stratification. This process acts in addition to advection-driven tidal straining and is based on the temporal covariance between eddy diffusivity and vertical salinity

gradients, as shown in (A24). The underlying process is the suppression of vertical turbulent salinity fluxes during times of strong stratification and vice versa. For weak stratification, s-ESCO dominates both free-surface and ice-covered estuaries (Figs. 5b,d) and contributes to 82% and 70% to the potential energy anomaly, respectively (Table 2). For the strong stratification scenario, the role of s-ESCO in generating residual stratification is much smaller than the major balance between gravitational circulation as stratifying agent and ESCO advection and nudging as destratifying agents (Fig. 7b). However, for the ice-covered scenario it is as strong as gravitational circulation (Fig. 7d). In addition to stratification (as expressed by the Simpson number Si), s-ESCO is also strongly depending on the nondimensional tidal frequency (as expressed by the unsteadiness number Un). With increasing Un (higher frequency) this process is less efficient. This can be interpreted in a way that sufficient time is needed for building up the vertical structure of the water column after slack tide in order to allow for the full effect of turbulence damping on stratification.

### e. *Perspectives for future work*

The major results of this highly idealized one-dimensional model study show that landfast sea ice cover on tidal estuaries changes the dynamics drastically. Estuarine circulation as well as stratification are predicted to be strongly reduced. The way how dynamics would be changed in real estuaries needs to be investigated with three-dimensional numerical models of real Arctic estuaries. Relevant effects of topography, specifically the channel–shoal interaction, Earth rotation, and channel curvature would further strongly modify the processes that have been shown here. As it is standard in estuarine research, the inclusion of turbulence closure models based on the TKE equation would be required to reproduce and quantify the effects of ESCO and s-ESCO. This is what the one-dimensional model results clearly show. In future three-dimensional model studies, the temperature equation as well as dynamic sea ice models should be included to study the effects of Arctic warming on estuarine sea ice reduction and its consequences for estuarine functioning in the Arctic.

In recent years, progress has been made in the modeling of ice-covered estuaries. Detailed model simulations have been carried out for ice-covered estuarine dynamics for example in parts of the Baltic Sea (Westerlund et al. 2019; Idzelytė et al. 2020) or the Gulf of Saint Lawrence (Long et al. 2016; Wang et al. 2018). In terms of high-resolution parameterization of melting and freezing processes under glacial ice tongues, progress has been recently made using turbulence closure models (Jenkins 2021; Burchard et al. 2022). With this, the required modeling techniques for realistic simulations of tidal estuaries covered by landfast sea ice are at hand. Additionally, field observations of the tidal dynamics under estuarine landfast sea ice cover are urgently needed to gain quantitative process understanding and to obtain validation data for numerical models. The tidal freshwater study by Georgas (2012) was a first step toward such field observations and model simulations.

## 7. Conclusions

Although some of the largest estuaries in the world are covered during about half of the year by landfast sea ice (section 2), a systematic characterization of their estuarine dynamics has not yet been made. The only other study (Georgas 2012) that systematically investigated the effects of landfast sea ice on tidal flow was carried out upstream of the salt intrusion. The present study is meant as a first step to extend the study by (Georgas 2012) to the estuarine parameter space including effects of horizontal density gradients. For situations without influence of horizontal salinity gradients, the present study could confirm the results by (Georgas 2012) who showed the effect of the no-slip surface boundary condition by means of field observations and three-dimensional model results.

In classical free-surface estuaries, generation processes of estuarine circulation and estuarine stratification have been a focus during the last seven decades (Pritchard 1952; Hansen and Rattray 1965; Ianniello 1979; Simpson et al. 1990; Jay and Musiak 1994; MacCready 2004; Stacey et al. 2010; Burchard and Hetland 2010; Lange and Burchard 2019). One fundamental method of analysis is based on the decomposition of tidally averaged profiles of momentum and salinity into contributions from terms in the momentum budget (section 1), using one-dimensional analytical or numerical water-column models. Such an analysis is applied here to juxtapose free-surface and ice-covered estuaries. The result is that landfast sea ice cover substantially changes the estuarine dynamics (section 6). The major process is a surface-stress related component that opposes classical estuarine circulation in a way comparable to landward wind stress forcing.

One-dimensional models are highly idealized by assuming among others horizontal homogeneity and constant horizontal buoyancy gradients and can therefore only give some first quantitative orientation of the underlying dynamics. Many of these insights from one-dimensional models have, however, been supported by field observations (Simpson et al. 2002; Becherer et al. 2016) or realistic model simulations (Scully et al. 2009; Scully and Geyer 2012; Lange et al. 2020). To add some generality to the water-column simulations used here, a large parameter space spanned by the Simpson number and the unsteadiness number is studied, covering unstratified and stratified estuaries of various tidal intensity. To enforce tidally periodic simulations and avoid runaway stratification, nudging to a constant salinity has been applied. It should be noted that in simulations with realistic estuarine bathymetry periodic forcing would lead to periodic results after some time. Salinity nudging is meant to parameterize the processes that lead to periodicity. To gain a more robust understanding of Arctic estuaries, future studies should include field observations and three-dimensional idealized and realistic model simulations.

Such a fundamental understanding is needed to predict changes in Arctic coastal regions that are triggered by the accelerated warming induced by Arctic amplification. This would also require conducting multiannual model simulations that include the melting and freezing periods during spring and autumn, which would lead to additional destabilization

(spring) and stabilization (autumn) of the water column. For this, more realistic site-specific three-dimensional model studies would be required.

*Acknowledgments.* The present study has been supported by the projects CoastalFutures (Grant 03F0911B; H. B. and X. L.) and GROCE-II (Grant 03F0855E; H. B.), both funded by the German Federal Ministry of Education and Research, as well as by the Ministry of Science and Higher Education of the Russian Federation (theme FMWE-2021-0001; A. O.). We are grateful for the constructive, precise, and in-depth comments by two anonymous reviewers.

*Data availability statement.* All simulations have been carried out by means of the GOTM, which can be freely downloaded at www.gotm.net. Further information on the model setups and analysis tools can be obtained directly from the authors.

## APPENDIX

### Decomposition of Residual Velocity and Salinity Anomaly Profiles

#### *a. Temporally constant eddy coefficients*

##### 1) VELOCITY PROFILES

The assumption of a stationary eddy viscosity $A_v = \langle A_v \rangle$ in (3) leads to

$$\partial_z(A_v \partial_z \langle u \rangle) = g\partial_x \langle \eta \rangle + z b_x. \tag{A1}$$

With constant eddy viscosity $A_v$, the flux condition (4) at the surface and the no-slip condition (5) at the bed, the solution for the velocity profile is obtained as

$$\langle u(z) \rangle = \underbrace{\left[8\left(\frac{z}{H}\right)^3 + 9\left(\frac{z}{H}\right)^2 - 1\right]u_g}_{\text{gravitational circulation}} + \underbrace{\left[3\left(\frac{z}{H}\right)^2 + 4\left(\frac{z}{H}\right) + 1\right]u_s}_{\text{surface stress circulation}} + \underbrace{\frac{3}{2}\left[1 - \left(\frac{z}{H}\right)^2\right]u^r}_{\text{river discharge}} \tag{A2}$$

with the exchange velocity due to gravitational circulation, $u_g = (b_x H^3)/(48A_v)$, and the exchange velocity due to surface-stress circulation, $u_s = u_{*,s}|u_{*,s}|H/(4A_v)$.

All terms in (A2) fulfill the no-slip bottom boundary condition $\langle u \rangle(-H) = 0$. Furthermore, the first two terms integrate to zero (in the sense that they are exchange profiles) and the depth-average of the last term is $u^r$. In (A2), the velocity shear at the bottom is

$$\partial_z u(-H) = \frac{1}{H}(6u_g - 2u_s + 3u^r), \tag{A3}$$

such that classical estuarine circulation with $\partial_z u(-H) > 0$ is obtained for

$$6u_g - 2u_s > -3u^r \tag{A4}$$

(note that $u^r \le 0$). Thus, gravitational circulation needs to exceed a certain strength to overcome the runoff circulation. This means additionally that a strong landward surface stress with $u_s > 0$ can create reverse estuarine circulation with $\partial_z u(-H) < 0$.

To represent the presence of landfast sea ice the no-slip condition $u(0) = 0$ and thus $\langle u(0) \rangle = 0$ at the surface is obtained by

$$u_s = u_g - \frac{3}{2}u^r, \tag{A5}$$

which gives with (A2) the tidally averaged velocity profile for an estuary covered with landfast ice

$$\langle u(z) \rangle = \underbrace{\left(\frac{z}{H}\right)\left[8\left(\frac{z}{H}\right)^2 + 12\left(\frac{z}{H}\right) + 4\right]u_g}_{\text{gravitational circulation}} \underbrace{- 6\left[\left(\frac{z}{H} + 0.5\right)^2 - 0.25\right]u^r}_{\text{river discharge}}. \tag{A6}$$

In (A6) it becomes clear that the flow part related to river discharge is symmetric around the middepth at $z = -H/2$.

Inserting (A5) into the condition for classical estuarine circulation (A4) gives the condition

$$u_g > 0, \tag{A7}$$

which means that adding landfast sea ice to a classical estuarine circulation situation will not reverse the sense of the estuarine circulation.

##### 2) SALINITY ANOMALY PROFILES

Assuming temporally constant eddy diffusivity and no nudging toward a target salinity ($T_n \to \infty$), (13) gives

$$\frac{\Delta s}{T} + \langle u \rangle s_x - \partial_z(K_v \partial_z \langle s \rangle) = 0, \tag{A8}$$

with the shift in salinity during one tidal cycle, $\Delta s$, that is assumed to be depth-independent. To eliminate $\Delta s$, (A8) is vertically integrated over the full water depth, using the boundary conditions (9), such that (13) can be reformulated as

$$\partial_z(K_v \partial_z \langle s \rangle) = (\langle u \rangle - u^r)s_x, \tag{A9}$$

where (7) has been used.

Two subsequent integrations of (A9) from a position $z$ in the water column to the surface lead to

$$\langle s(z) \rangle = \langle s(0) \rangle + \left[\int_z^0 \int_{z'}^0 \langle u(z'') \rangle dz'' dz' - \frac{z^2}{2}u^r\right]\frac{s_x}{K_v}. \tag{A10}$$

With the definition of the salinity anomaly,

$$\langle \tilde{s}(z) \rangle = \langle s(z) \rangle - \frac{1}{H}\int_{-H}^0 \langle s(z) \rangle dz, \tag{A11}$$

the salinity anomaly is given as

$$\langle \tilde{s}(z)\rangle = \left\{\frac{1}{H^2}\int_z^0\int_{z'}^0\langle u(z'')\rangle dz''dz' - \frac{1}{H^3}\int_{-H}^0\int_z^0\int_{z'}^0\langle u(z'')\rangle dz''dz'dz\right.$$
$$= -\frac{1}{2}\left[\left(\frac{z}{H}\right)^2 - \frac{1}{3}\right]u^r\Bigg\}\frac{s_x H^2}{K_v}\left[\frac{2}{5}\left(\frac{z}{H}\right)^5 + \frac{3}{4}\left(\frac{z}{H}\right)^4 - \frac{1}{2}\left(\frac{z}{H}\right)^2 + \frac{1}{12}\right]s_g$$
$$+\left[\frac{1}{4}\left(\frac{z}{H}\right)^4 + \frac{2}{3}\left(\frac{z}{H}\right)^3 + \frac{1}{2}\left(\frac{z}{H}\right)^2 - \frac{1}{20}\right]s_w$$
$$+\left[\frac{1}{8}\left(\frac{z}{H}\right)^4 - \frac{1}{4}\left(\frac{z}{H}\right)^2 + \frac{7}{120}\right]s_r, \tag{A12}$$

with the salinities

$$s_g = u_g\frac{s_x H^2}{K_v} = -\frac{b_x^2 \mathrm{Pr}^t H^5}{48A_v^2 g\beta},$$
$$s_w = u_s\frac{s_x H^2}{K_v} = -\frac{u_{*,s}|u_{*,s}|b_x \mathrm{Pr}^t H^3}{4A_v^2 g\beta}, \tag{A13}$$
$$s_r = -u^r\frac{s_x H^2}{K_v} = \frac{u^r b_x \mathrm{Pr}^t H^2}{A_v g\beta}.$$

To obtain salinity anomaly profiles for landfast sea ice, condition (A5) must be additionally applied.

*b. Time-varying eddy coefficients*

1) VELOCITY PROFILES

Using

$$\langle A_v\partial_z u\rangle = \langle A_v\rangle\partial_z\langle u\rangle + \langle A_{v'}\partial_z u'\rangle, \tag{A14}$$

where the second term on the right-hand side denotes ECSO, (3) can be formally solved as

$$\langle u(z)\rangle = \sum_{i=1}^3\left[\int_{-H}^z \mathcal{A}_i(\xi)d\xi - \frac{\gamma(z)}{H}\int_{-H}^0\int_{-H}^z \mathcal{A}_i(\xi)d\xi\, dz\right] - \gamma(z)u^r$$
$$\equiv \sum_{i=1}^3\langle u_i(z)\rangle - \langle u_4(z)\rangle, \tag{A15}$$

with the terms

$$\mathcal{A}_1(z) = -\frac{\langle A_{v'}(z)\partial_z u'(z)\rangle}{\langle A_v(z)\rangle}, \quad \mathcal{A}_2(z) = \frac{z^2 b_x}{2\langle A_v(z)\rangle},$$
$$\mathcal{A}_3(z) = \frac{\langle u_{*,s}|u_{*,s}|\rangle}{\langle A_v(z)\rangle}, \tag{A16}$$

and the nondimensional residual runoff velocity profile

$$\gamma(z) = \frac{H\displaystyle\int_{-H}^z \frac{\xi}{\langle A_v(\xi)\rangle}\,d\xi}{\displaystyle\int_{-H}^0\int_{-H}^z \frac{\xi}{\langle A_v(\xi)\rangle}\,d\xi\,dz}, \tag{A17}$$

see Burchard and Hetland (2010) for details of the derivation. In (A15), $\langle u_1(z)\rangle$ is the contribution from ESCO, $\langle u_2(z)\rangle$ is the contribution from gravitational circulation and $\langle u_3(z)\rangle$ is the contribution from surface stress. The bottom boundary value of $\mathcal{A}_1$ is based on the following law-of-the-wall relations:

$$A_v(-H) = \kappa z_0^b|u_{*,b}|, \quad \partial_z u(-H) = \frac{u_{*,b}}{\kappa z_0^b} \quad \text{for } z = -H, \tag{A18}$$

with the van Kármán constant $\kappa = 0.4$ and the bottom roughness parameter $z_0^b$. With (A18),

$$\langle A_v(-H)\rangle = \kappa z_0^b\langle|u_{*,b}|\rangle,$$
$$\langle A_v(-H)\partial_z u(-H)\rangle = \langle|u_{*,b}|u_{*,b}\rangle, \tag{A19}$$
$$\langle A_v(-H)\rangle\partial_z\langle u(-H)\rangle = \langle|u_{*,b}|\rangle\langle u_{*,b}\rangle,$$

is obtained such that

$$\mathcal{A}_1(-H) = \frac{\langle|u_{*,b}|\rangle\langle u_{*,b}\rangle - \langle|u_{*,b}|u_{*,b}\rangle}{\kappa z_0^b\langle|u_{*,b}|\rangle} = \frac{\langle|u_{*,b}|\rangle\langle u_{*,b}\rangle - \dfrac{\langle\tau_b\rangle}{\rho_0}}{\kappa z_0^b\langle|u_{*,b}|\rangle}. \tag{A20}$$

2) SALINITY ANOMALY PROFILES

Starting from (13), and carrying out two subsequent integrations from $z' = z$ to $z' = 0$, the residual salinity profile can be decomposed as

$$\langle s(z)\rangle - \langle s(0)\rangle = \sum_{i=1}^6\langle s_i(z)\rangle, \tag{A21}$$

where

$$\langle s_i(z)\rangle = \int_z^0\frac{s_x}{\langle K_v\rangle}\int_{z'}^0\langle u_i(z'')\rangle dz''dz' \quad \text{for } i = 1,\ldots,3 \tag{A22}$$

are the residual salinity profiles due to ESCO, gravitational circulation and surface stress, respectively,

$$\langle s_4(z)\rangle = \int_z^0\left\{\frac{u^r s_x}{\langle K_v\rangle}\int_{z'}^0[\gamma(z'') - 1]\,dz''\right\}dz' \tag{A23}$$

is the residual salinity profile due to river runoff and

$$\langle s_5(z)\rangle = \int_z^0\frac{\langle K_v'\partial_z s'\rangle}{\langle K_v\rangle}\,dz' \tag{A24}$$

is the residual salinity profile due to s-ESCO. Furthermore, the nudging term results as

$$\langle s_6(z)\rangle = \frac{1}{T_n}\int_z^0\frac{1}{\langle K_v\rangle}\int_{z'}^0[\langle s(z'')\rangle - \overline{\langle s\rangle}]\,dz''dz'. \tag{A25}$$

Finally, the decomposition of the residual salinity anomaly profile is obtained by

$$\langle\tilde{s}_i(z)\rangle = \langle s_i(z)\rangle - \frac{1}{H}\int_{-H}^0\langle s_i(z')\rangle\,dz' \quad \text{for } i = 1,\ldots,6. \tag{A26}$$

## REFERENCES


Baumert, H., and G. Radach, 1992: Hysteresis of turbulent kinetic energy in nonrotational tidal flows: A model study. *J. Geophys. Res.*, **97**, 3669–3677, https://doi.org/10.1029/91JC02717.

Becherer, J., G. Flöser, L. Umlauf, and H. Burchard, 2016: Estuarine circulation versus tidal pumping: Sediment transport in a well-mixed tidal inlet. *J. Geophys. Res. Oceans*, **121**, 6251–6270, https://doi.org/10.1002/2016JC011640.

Blaise, S., and E. Deleersnijder, 2008: Improving the parameterisation of horizontal density gradient in one-dimensional water column models for estuarine circulation. *Ocean Sci.*, **4**, 239–246, https://doi.org/10.5194/os-4-239-2008.

Burchard, H., 2009: Combined effects of wind, tide, and horizontal density gradients on stratification in estuaries and coastal seas. *J. Phys. Oceanogr.*, **39**, 2117–2136, https://doi.org/10.1175/2009JPO4142.1.

——, and H. Baumert, 1998: The formation of estuarine turbidity maxima due to density effects in the salt wedge. A hydrodynamic process study. *J. Phys. Oceanogr.*, **28**, 309–321, https://doi.org/10.1175/1520-0485(1998)028<0309:TFOETM>2.0.CO;2.

——, and K. Bolding, 2001: Comparative analysis of four second-moment turbulence closure models for the oceanic mixed layer. *J. Phys. Oceanogr.*, **31**, 1943–1968, https://doi.org/10.1175/1520-0485(2001)031<1943:CAOFSM>2.0.CO;2.

——, and R. Hofmeister, 2008: A dynamic equation for the potential energy anomaly for analysing mixing and stratification in estuaries and coastal seas. *Estuarine Coastal Shelf Sci.*, **77**, 679–687, https://doi.org/10.1016/j.ecss.2007.10.025.

——, and R. D. Hetland, 2010: Quantifying the contributions of tidal straining and gravitational circulation to residual circulation in periodically stratified tidal estuaries. *J. Phys. Oceanogr.*, **40**, 1243–1262, https://doi.org/10.1175/2010JPO4270.1.

——, K. Bolding, and M. R. Villarreal, 1999: GOTM—A general ocean turbulence model: Theory, applications and test cases. European Commission Tech. Rep. EUR 18745 EN, 103 pp.

——, R. D. Hetland, E. Schulz, and H. M. Schuttelaars, 2011: Drivers of residual circulation in tidally energetic estuaries: Straight and irrotational estuaries with parabolic cross-section. *J. Phys. Oceanogr.*, **41**, 548–570, https://doi.org/10.1175/2010JPO4453.1.

——, E. Schulz, and H. M. Schuttelaars, 2014: Impact of estuarine convergence on residual circulation in tidally energetic estuaries and inlets. *Geophys. Res. Lett.*, **41**, 913–919, https://doi.org/10.1002/2013GL058494.

——, H. M. Schuttelaars, and D. K. Ralston, 2018: Sediment trapping in estuaries. *Annu. Rev. Mar. Sci.*, **10**, 371–395, https://doi.org/10.1146/annurev-marine-010816-060535.

——, K. Bolding, A. Jenkins, M. Losch, M. Reinert, and L. Umlauf, 2022: The vertical structure and entrainment of subglacial melt water plumes. *J. Adv. Model Earth Syst.*, **14**, e2021MS002925, https://doi.org/10.1029/2021MS002925.

Chen, S.-N., and L. P. Sanford, 2009: Axial wind effects on stratification and longitudinal salt transport in an idealized, partially mixed estuary. *J. Phys. Oceanogr.*, **39**, 1905–1920, https://doi.org/10.1175/2009JPO4016.1.

Chernov, I., P. Lazzari, A. Tolstikov, M. Kravchishina, and N. Iakovlev, 2018: Hydrodynamical and biogeochemical spatiotemporal variability in the White Sea: A modeling study. *J. Mar. Syst.*, **187**, 23–35, https://doi.org/10.1016/j.jmarsys.2018.06.006.

Dai, A., and K. E. Trenberth, 2002: Estimates of freshwater discharge from continents: Latitudinal and seasonal variations. *J. Hydrometeor.*, **3**, 660–687, https://doi.org/10.1175/1525-7541(2002)003<0660:EOFDFC>2.0.CO;2.

Dijkstra, Y. M., H. M. Schuttelaars, and H. Burchard, 2017: Generation of exchange flows in estuaries by tidal and gravitational eddy viscosity-shear covariance (ESCO). *J. Geophys. Res. Oceans*, **122**, 4217–4237, https://doi.org/10.1002/2016JC012379.

Georgas, N., 2012: Large seasonal modulation of tides due to ice cover friction in a midlatitude estuary. *J. Phys. Oceanogr.*, **42**, 352–369, https://doi.org/10.1175/JPO-D-11-063.1.

Geyer, W. R., 1997: Influence of wind on dynamics and flushing of shallow estuaries. *Estuarine Coastal Shelf Sci.*, **44**, 713–722, https://doi.org/10.1006/ecss.1996.0140.

——, and P. MacCready, 2014: The estuarine circulation. *Annu. Rev. Fluid Mech.*, **46**, 175–197, https://doi.org/10.1146/annurev-fluid-010313-141302.

Gordeev, V. V., J. M. Martin, J. S. Sidorov, and M. V. Sidorova, 1996: A reassessment of the Eurasian river input of water, sediment, major elements, and nutrients to the Arctic Ocean. *Amer. J. Sci.*, **296**, 664–691, https://doi.org/10.2475/ajs.296.6.664.

Hansen, D. V., and M. Rattray, 1965: Gravitational circulation in straits and estuaries. *J. Mar. Res.*, **23**, 104–122.

Herrling, G., M. Becker, A. Lefebvre, A. Zorndt, K. Krämer, and C. Winter, 2021: The effect of asymmetric dune roughness on tidal asymmetry in the Weser estuary. *Earth Surf. Processes Landforms*, **46**, 2211–2228, https://doi.org/10.1002/esp.5170.

Ianniello, J. P., 1979: Tidally induced residual currents in estuaries of variable breadth and depth. *J. Phys. Oceanogr.*, **9**, 962–974, https://doi.org/10.1175/1520-0485(1979)009<0962:TIRCIE>2.0.CO;2.

Idzelytė, R., J. Mėžinė, P. Zemlys, and G. Umgiesser, 2020: Study of ice cover impact on hydrodynamic processes in the Curonian Lagoon through numerical modeling. *Oceanologia*, **62**, 428–442, https://doi.org/10.1016/j.oceano.2020.04.006.

Jay, D. A., and J. D. Musiak, 1994: Particle trapping in estuarine tidal flows. *J. Geophys. Res.*, **99**, 20 445–20 461, https://doi.org/10.1029/94JC00971.

Jenkins, A., 2021: Shear, stability and mixing within the ice-shelf-ocean boundary current. *J. Phys. Oceanogr.*, **51**, 2129–2148, https://doi.org/10.1175/JPO-D-20-0096.1.

Kulikov, M. E., I. P. Medvedev, and A. T. Kondrin, 2020: Features of seasonal variability of tidal sea-level oscillations in the Russian Arctic Seas. *Russ. Meteor. Hydrol.*, **45**, 411–421, https://doi.org/10.3103/S1068373920060047.

Lange, X., and H. Burchard, 2019: The relative importance of wind straining and gravitational forcing in driving exchange flows in tidally energetic estuaries. *J. Phys. Oceanogr.*, **49**, 723–736, https://doi.org/10.1175/JPO-D-18-0014.1.

——, K. Klingbeil, and H. Burchard, 2020: Inversions of estuarine circulation are frequent in a weakly tidal estuary with variable wind forcing and seaward salinity fluctuations. *J. Geophys. Res. Oceans*, **125**, e2019JC015789, https://doi.org/10.1029/2019JC015789.

Lerczak, J. A., and W. R. Geyer, 2004: Modelling the lateral circulation in straight, stratified estuaries. *J. Phys. Oceanogr.*, **34**, 1410–1428, https://doi.org/10.1175/1520-0485(2004)034<1410:MTLCIS>2.0.CO;2.

Li, Q., J. Bruggeman, H. Burchard, K. Klingbeil, L. Umlauf, and K. Bolding, 2021: Integrating CVMix into GOTM (v6. 0): A consistent framework for testing, comparing, and applying ocean mixing schemes. *Geosci. Model Dev.*, **14**, 4261–4282, https://doi.org/10.5194/gmd-14-4261-2021.

Long, Z., W. Perrie, J. Chassé, D. Brickman, L. Guo, A. Drozdowski, and H. Hu, 2016: Impacts of climate change in the Gulf of

St. Lawrence. *Atmos.–Ocean*, **54**, 337–351, https://doi.org/10.1080/07055900.2015.1029869.

MacCready, P., 2004: Toward a unified theory of tidally-averaged estuarine salinity structure. *Estuaries*, **27**, 561–570, https://doi.org/10.1007/BF02907644.

——, and W. R. Geyer, 2010: Advances in estuarine physics. *Annu. Rev. Mar. Sci.*, **2**, 35–58, https://doi.org/10.1146/annurev-marine-120308-081015.

Macdonald, R. W., and Y. Yu, 2006: The Mackenzie Estuary of the Arctic Ocean. *Estuaries*, P. J. Wangersky, Eds., *The Handbook of Environmental Chemistry*, Vol. 5H, Springer, 91–120, https://doi.org/10.1007/698_5_027.

McPhee, M. G., G. A. Maykut, and J. H. Morison, 1987: Dynamics and thermodynamics of the ice/upper ocean system in the marginal ice zone of the Greenland Sea. *J. Geophys. Res.*, **92**, 7017–7031, https://doi.org/10.1029/JC092iC07p07017.

Mellor, G. L., and L. Kantha, 1989: An ice-ocean coupled model. *J. Geophys. Res.*, **94**, 10 937–10 954, https://doi.org/10.1029/JC094iC08p10937.

Mohammadian, A., B. Morse, and J.-L. Robert, 2021: Winter impacts on cryo-hydrodynamics of an Arctic hypertidal estuary: Implications on tidal-stream energy. *J. Ocean Eng. Mar. Energy*, **7**, 459–479, https://doi.org/10.1007/s40722-021-00207-w.

Monismith, S. G., J. R. Burau, and M. T. Stacey, 1996: Stratification dynamics and gravitational circulation in Northern San Francisco Bay. *San Francisco Bay: The Ecosystem*, J. T. Hollibaugh, Ed., American Association for the Advancement of Science Pacific Division, 123–153.

Nunes, R. A., and J. H. Simpson, 1985: Axial convergence in a well-mixed estuary. *Estuarine Coastal Shelf Sci.*, **20**, 637–649, https://doi.org/10.1016/0272-7714(85)90112-X.

Osadchiev, A. A., E. E. Asadulin, A. Y. Miroshnikov, I. B. Zavialov, E. O. Dubinina, and P. A. Belyakova, 2019: Bottom sediments reveal inter-annual variability of interaction between the Ob and Yenisei plumes in the Kara Sea. *Sci. Rep.*, **9**, 18642, https://doi.org/10.1038/s41598-019-55242-3.

——, I. Medvedev, S. Shchuka, M. Kulikov, E. Spivak, M. Pisareva, and I. Semiletov, 2020a: Influence of estuarine tidal mixing on structure and spatial scales of large river plumes. *Ocean Sci.*, **16**, 781–798, https://doi.org/10.5194/os-16-781-2020.

——, K. Silvestrova, and S. Myslenkov, 2020b: Wind-driven coastal upwelling near large river deltas in the Laptev and East-Siberian seas. *Remote Sens.*, **12**, 844, https://doi.org/10.3390/rs12050844.

——, D. Frey, E. Spivak, S. Shchuka, N. Tilinina, and I. Semiletov, 2021a: Structure and inter-annual variability of the freshened surface layer in the Laptev and East-Siberian seas during ice-free periods. *Front. Mar. Sci.*, **8**, 735011, https://doi.org/10.3389/fmars.2021.735011.

——, O. Konovalova, and A. Gordey, 2021b: Water exchange between the Gulf of Ob and the Kara Sea during ice-free seasons: The roles of river discharge and wind forcing. *Front. Mar. Sci.*, **8**, 741143, https://doi.org/10.3389/fmars.2021.741143.

——, D. I. Frey, S. A. Shchuka, N. D. Tilinina, E. G. Morozov, and P. O. Zavialov, 2021c: Structure of the freshened surface layer in the Kara Sea during ice-free periods. *J. Geophys. Res. Oceans*, **126**, e2020JC016486, https://doi.org/10.1029/2020JC016486.

Pavlov, V., L. Timokhov, G. Baskakov, Y. Kulakov, V. Kurazhov, P. Pavlov, S. Pivovarov, and V. Stanovoy, 1996: Hydrometeorological regime of the Kara, Laptev, and East-Siberian seas. Tech. Memo. APL-UW TM 1-96, 185 pp.

Popov, A. V., N. V. Kubishkin, A. V. Rubchenia, and D. V. Drabenko, 2016: Dynamics of the edge of the soldered sagebrush in the Gulf of Ob and the forecast of its latitudinal position. *Ice Snow*, **56**, 387–398, https://doi.org/10.15356/2076-6734-2016-3-387-398.

Pritchard, D. W., 1952: Salinity distribution and circulation in the Chesapeake Bay estuarine system. *J. Mar. Res.*, **11**, 106–123.

——, 1954: A study of the salt balance in a coastal plain estuary. *J. Mar. Res.*, **13**, 133–144.

——, 1956: The dynamic structure of a coastal plane estuary. *J. Mar. Res.*, **15**, 33–42.

Rippeth, T. P., N. R. Fisher, and J. H. Simpson, 2001: The cycle of turbulent dissipation in the presence of tidal straining. *J. Phys. Oceanogr.*, **31**, 2458–2471, https://doi.org/10.1175/1520-0485(2001)031<2458:TCOTDI>2.0.CO;2.

Scully, M. E., and W. R. Geyer, 2012: The role of advection, straining, and mixing on the tidal variability of estuarine stratification. *J. Phys. Oceanogr.*, **42**, 855–868, https://doi.org/10.1175/JPO-D-10-05010.1.

——, ——, and J. A. Lerczak, 2009: The influence of lateral advection on the residual estuarine circulation: A numerical modeling study of the Hudson River estuary. *J. Phys. Oceanogr.*, **39**, 107–124, https://doi.org/10.1175/2008JPO3952.1.

Simpson, J. H., 1981: The shelf-sea fronts: Implications of their existence and behaviour. *Philos. Trans. Roy. Soc.*, **A302**, 531–546, https://doi.org/10.1098/rsta.1981.0181.

——, J. Brown, J. Matthews, and G. Allen, 1990: Tidal straining, density currents, and stirring in the control of estuarine stratification. *Estuaries*, **13**, 125–132, https://doi.org/10.2307/1351581.

——, H. Burchard, N. R. Fisher, and T. P. Rippeth, 2002: The semidiurnal cycle of dissipation in a ROFI: Model-measurement comparisons. *Cont. Shelf Res.*, **22**, 1615–1628, https://doi.org/10.1016/S0278-4343(02)00025-0.

Spivak, E. A., A. A. Osadchiev, and I. P. Semiletov, 2021: Structure and variability of the Lena River plume in the southeastern part of the Laptev Sea. *Oceanology*, **61**, 839–849, https://doi.org/10.1134/S000143702106014X.

Stacey, M. T., M. L. Brennan, J. R. Burau, and S. G. Monismith, 2010: The tidally averaged momentum balance in a partially and periodically stratified estuary. *J. Phys. Oceanogr.*, **40**, 2418–2434, https://doi.org/10.1175/2010JPO4389.1.

Tarasenko, A., V. Selyuzhenok, N. Sandalyuk, I. A. Abramova, and D. M. Demchev, 2022: A study of sea ice regime in the Obskaya Guba Bay using modern satellite data in 2007–2017. *Arct. Antarct. Res.*, **68**, 48–63, https://doi.org/10.30758/0555-2648-2021-68-1-48-63.

Umlauf, L., and H. Burchard, 2005: Second-order turbulence closure models for geophysical boundary layers. A review of recent work. *Cont. Shelf Res.*, **25**, 795–827, https://doi.org/10.1016/j.csr.2004.08.004.

Voinov, G., 2016: Tides in the Gulf of Ob (Kara Sea). II. The influence of ice cover on the characteristics of the tides. *Proc. Russ. State Hydrometeor. Univ.*, **45**, 43–63.

——, and A. A. Piskun, 2019: Tidal and storm surges levels variation at the Cape Kamenny (Gulf of Ob). *Arct. Antarct. Res.*, **65**, 15–33, https://doi.org/10.30758/0555-2648-2019-65-1-15-33.

——, Y. Nalimov, A. Piskun, V. Stanovoy, and G. Usankina, 2017: *Main Features of the Hydrological Regime of the Ob and Taz Gulfs (Ice, Level, Water Structure)*. Nestor-Istoriya, 192 pp.

Wang, L., W. Perrie, Z. Long, M. Blokhina, G. Zhang, B. Toulany, and M. Zhang, 2018: The impact of climate change on the wave climate in the Gulf of St. Lawrence. *Ocean Modell.*, **128**, 87–101, https://doi.org/10.1016/j.ocemod.2018.06.003.

Wang, R., G. K. McCullough, G. G. Gunn, K. P. Hochheim, A. Dorostkar, K. Sydor, and D. G. Barber, 2012: An observational study of ice effects on Nelson River estuarine variability, Hudson Bay, Canada. *Cont. Shelf Res.*, **47**, 68–77, https://doi.org/10.1016/j.csr.2012.06.014.

Weisberg, R. H., and W. Sturges, 1976: Velocity observations in the west passage of Narragansett Bay: A partially mixed estuary. *J. Phys. Oceanogr.*, **6**, 345–354, https://doi.org/10.1175/1520-0485(1976)006<0345:VOITWP>2.0.CO;2.

Westerlund, A., L. Tuomi, P. Alenius, K. Myrberg, E. Miettunen, R. E. Vankevich, and R. Hordoir, 2019: Circulation patterns in the Gulf of Finland from daily to seasonal timescales. *Tellus*, **71A**, 1627149, https://doi.org/10.1080/16000870.2019.1627149.

Wright, L. D., D. B. Prior, C. H. Hobbs, R. J. Byrne, J. D. Boon, L. C. Schaffner, and M. O. Green, 1987: Spatial variability of bottom types in the lower Chesapeake Bay and adjoining estuaries and inner shelf. *Estuarine Coastal Shelf Sci.*, **24**, 765–784, https://doi.org/10.1016/0272-7714(87)90151-X.